

# Probing time-dependent afterslip and viscoelastic relaxation following the 2015 Mw 7.8 Gorkha earthquake based on the 3-D Finite Element Model

Lina Su (✉ [sulinawhu@163.com](mailto:sulinawhu@163.com))

Shaanxi Earthquake Agency <https://orcid.org/0000-0002-7711-786X>

Fuqiang Shi

Shaanxi Earthquake Agency

Weijun Gan

China Earthquake Administration Institute of Geology

Xiaoning Su

faculty of Geomatics, Lanzhou Jiaotong University

Junyi Yan

Shaanxi Earthquake Agency

---

## Full paper

**Keywords:** GPS, 2015 Gorkha earthquake, postseismic deformation, afterslip, viscoelastic relaxation, finite element model

**Posted Date:** October 15th, 2020

**DOI:** <https://doi.org/10.21203/rs.3.rs-40078/v3>

**License:**  This work is licensed under a Creative Commons Attribution 4.0 International License.

[Read Full License](#)

---

**Version of Record:** A version of this preprint was published on November 4th, 2020. See the published version at <https://doi.org/10.1186/s40623-020-01296-x>.

# 1 Probing time-dependent afterslip and viscoelastic relaxation following 2 the 2015 Mw 7.8 Gorkha earthquake based on the 3-D Finite Element 3 Model

4 Lina Su<sup>1,2\*</sup>, Fuqiang Shi<sup>2</sup>, Weijun Gan<sup>1</sup>, Xiaoning Su<sup>3</sup>, Junyi Yan<sup>2</sup>

5 **Abstract:** We analyzed daily displacement time series from 34 continuous GPS stations in Nepal  
6 and 5 continuous GPS stations in South Tibet, China, and extracted the first 4.8 years of  
7 postseismic motion after the 2015 Mw7.8 Gorkha earthquake. With the longer duration GPS  
8 observations, we find that postseismic displacements mainly exhibit southward and uplift motion.  
9 To study the postseismic afterslip and viscoelastic relaxation, we built a 3-D spherical finite  
10 element model (FEM) with heterogeneous material properties and surface topography across the  
11 Himalayan range, accounting for the strong variations in material properties and surface elevation  
12 along central Himalayan arc. On the basis of the FEM, we reveal that the predicted viscoelastic  
13 relaxation of cm level moves southward to the north of the Gorkha earthquake rupture, but in an  
14 opposite direction to the observed postseismic deformation in the south; the postseismic  
15 deformation excluding viscoelastic relaxation is well explained by afterslip downdip of the  
16 coseismic rupture. The afterslip is dominant during 4.8 years after the 2015 Mw7.8 Gorkha  
17 earthquake; the contribution by the viscoelastic relaxation gradually increases slightly. The lack of  
18 slip on a shallow portion and western segment of the MHT during and after the 2015 Gorkha  
19 earthquake implies continued seismic hazard in the future.

20 **Keywords:** GPS; 2015 Gorkha earthquake; postseismic deformation; afterslip; viscoelastic  
21 relaxation; finite element model

## 22 1. introduction

23 On 25 April 2015, the Mw 7.8 Gorkha earthquake struck, just 77 km northwest of Kathmandu,  
24 Nepal, resulting in large economic losses and a death toll of up to 8000 (Earthquake Relief Portal,  
25 2015). The Himalayan region, accommodating a high convergence rate of 40-50 mm/yr between  
26 the overriding Eurasian Plate and the underthrusting Indian Plate (Bilham et al.,1997; Lavé &  
27 Avouac, 2000), is prone to earthquakes, such as the 1255 and 1934 Mw8+ Nepal-Bihar

\*Correspondence:sulinawhu@163.com 1. State Key Laboratory of Earthquake Dynamics, Institute of Geology, China Earthquake Administration, Beijing, 100029, China. 2. Shaanxi Earthquake Agency, Xi'an, 710068, China

28 earthquakes, 1956 Mw8.6 Assam-Tibet earthquake, 2005 Mw7.6 Kashmir earthquake, etc.  
29 (Sapkota et al.,2013; Bilham et al., 2004; Wang & Fialko,2014 ). The Gorkha earthquake occurred  
30 near the E-W trending Main Frontal Thrust (MFT) (USGS, 2015), the most active branch of the  
31 Main Himalayan Thrust (MHT), which absorbs about half of MHT convergence (Lavé & Avouac,  
32 2000; Kumar et al., 2001). Studies show that the 2015 Gorkha rupture was concentrated in the  
33 deeper part of the seismogenic zone, between depths of 10 and 15 km, leaving the unbroken  
34 shallow part at high seismic risk (Lindsey et al., 2015; Wang & Fialko, 2015; Mencin et al., 2016;  
35 Sreejith et al., 2016; Galetzka et al., 2015)

36 When an earthquake occurs, sudden coseismic stress changes in the surrounding rocks may  
37 lead to viscoelastic relaxation in the lower crust and upper mantle, and aseismic slip updip and/or  
38 downdip of the coseismic rupture (Pollitz et al., 2003; Freed et al., 2004,2007,2010; Rousset et al.,  
39 2012; Perfettini et al., 2004; Barbot et al., 2009; Savage and Svarc, 2009). The postseismic  
40 deformation due to the Gorkha earthquake provides valuable constraints to investigate the  
41 lithosphere strength and constitutive properties beneath the Himalayan region and Tibetan  
42 Plateau. Therefore, the exploration of postseismic transients and what mechanisms govern the  
43 postseismic process is of a broad interest. A few of studies focused on the afterslip modeling to  
44 explain the rapid transient postseismic deformation (Gualandi et al., 2016; Sreejith et al., 2016;  
45 Jiang et al., 2019). With the longer span of data available, some studies investigated various  
46 mechanical processes contributed by afterslip and viscoelastic relaxation with and without  
47 poroelastic rebound (Mencin et al., 2016; Zhao et al., 2017; Wang & Fialko, 2018; Jiang et al.,  
48 2018; Jouanne et al.,2019; Tian et al., 2020; Liu et al., 2020). The previous studies mostly  
49 employed the homogeneous elastic half-space or layered elastic model to explore afterslip  
50 (Sreejith et al., 2016; Zhao et al., 2017; Wang & Fialko, 2018; Jiang et al., 2018; Jiang et al., 2019),  
51 and the layered model or lateral heterogeneous model, which incorporates a low viscous layer  
52 beneath the Tibetan Plateau to investigate viscoelastic relaxation (Zhao et al., 2017; Wang & Fialko,  
53 2018; Jouanne et al., 2019; Tian et al., 2020).

54 Material heterogeneity affects surface deformation due to fault slip (Masterlark et al.,  
55 2001,2003; Hughes et al., 2010; Kyriakopoulos et al., 2013; Wiseman et al., 2015; Tung et al., 2016;  
56 Hu et al., 2016; Klein et al., 2016; Hsu et al., 2014; Hines et al., 2016; Pratama et al., 2017; Suito,

57 2017; Freed et al., 2017). Therefore, the homogenous or layered earth model assumption for the  
58 Himalayan range, which has strong variations in material properties (Cattin et al., 2001; Monsalve  
59 et al., 2006; Schul.te-Pelkum et al., 2005), inevitably introduces bias into the modelling  
60 (Kyriakopoulos et al., 2013; Tung et al., 2016; Suito, 2017; ). In this paper, we build a 3-D spherical  
61 finite element model (FEM) considering heterogeneous material properties and surface  
62 topography across the Himalayan range to investigate the aseismic afterslip and the viscoelastic  
63 relaxation following the 2015 Gorkha earthquake, using extracted postseismic displacement from  
64 continuous GPS (cGPS) data in Nepal and southern Tibetan Plateau over 4.8 years after the event.

## 65 **2. GPS data and postseismic deformation**

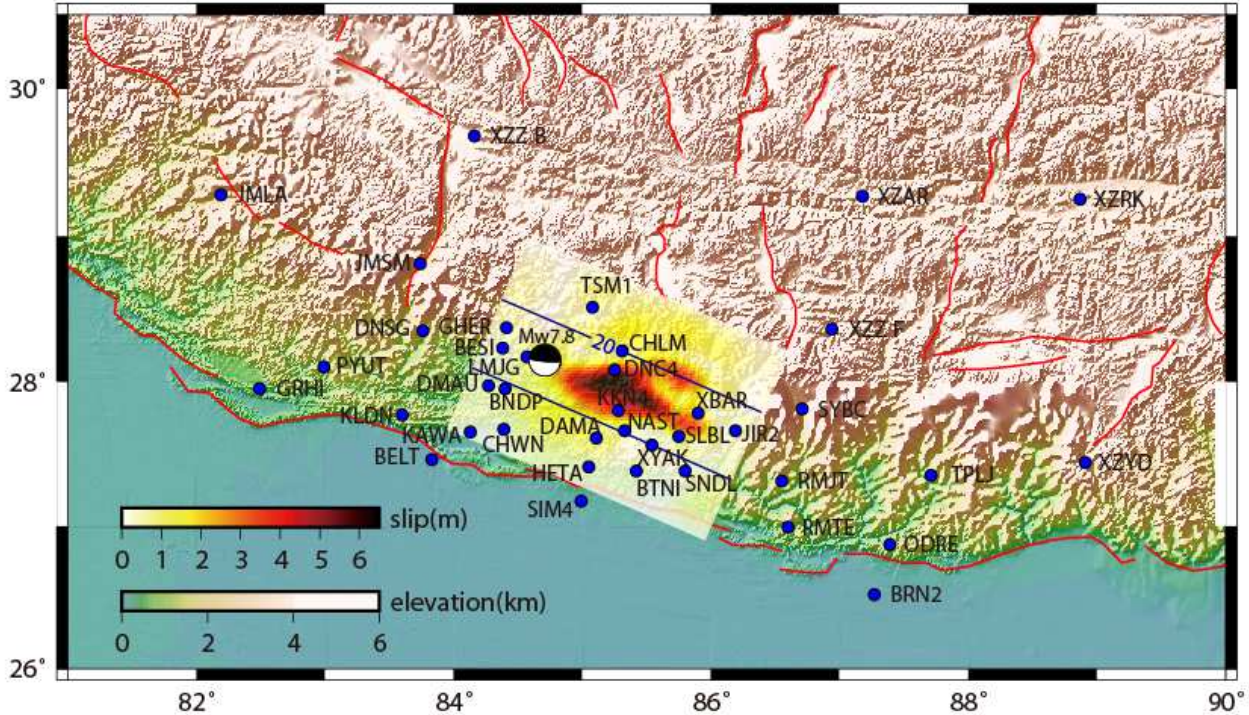
### 66 **2.1 GPS processing**

67 We collected raw RINEX data from 39 cGPS sites within an area between 78–92° E and 23–  
68 34°N (Fig.1). GPS sites in Nepal include 25 sites operated prior to the Gorkha earthquake and 9  
69 sites deployed immediately after the earthquake to capture postseismic deformation. The raw  
70 RINEX files of these sites are openly available at UNAVCO (<ftp://data-out.unavco.org>). We  
71 additionally collected data from 5 cGPS in South Tibet from the Crustal Movement Observation  
72 Network of China (CMONOC) (<http://www.cgps.ac.cn/>), which began recording in 2011.

73 We processed the GPS data using the GAMIT/GLOBK processing software (Herring, et al.,  
74 2015). Initially, we estimated loosely constrained daily solutions with GAMIT, together with orbits  
75 and Earth orientation, tropospheric delay parameters and full covariance matrices. We used data  
76 from the 39 cGPS sites from Nepal and South Tibet together with about 80 global distributed core  
77 stations of the International GNSS Service (Johnston et al., 2017). Then, we used GLOBK, a  
78 smoothing Kalman filter, to transform the loosely constrained solutions to the ITRF2014 reference  
79 frame (Altamimi et al., 2016), which is realized by the 80 core stations. The detailed strategy and  
80 applied models followed Su et al. (2019).

81 We estimated daily displacement time series for the 5 GPS sites in Tibet from 2011 until  
82 March 5, 2020, and 34 sites in Nepal from 2011 until January 26, 2019. We compared our time  
83 series with solutions from the Nevada Geodetic Laboratory (NGL) (Blewitt et al., 2018) and found  
84 the two data sets to be in good agreement (Fig. S1). Since the GPS coordinate time series for sites  
85 in Nepal routinely provided by NGL have longer duration, some of those begin in the 1990's, we

86 used in the time series modeling the NGL solutions for these sites. Considering the possible slight  
 87 deviation due to the different reference frame realizations of the two solutions, we estimated  
 88 seven transformation parameters between the NGL and our GAMT/GLOBK solutions to transfer  
 89 the NGL solutions from IGS 08 (Reischung et al., 2012) to ITRF2014.



90  
 91 **Fig. 1** Tectonic setting. The black beach ball shows the mainshock focal mechanism from U.S. Geological Survey. The blue circles are continuous GPS  
 92 sites used in this study. The color represents the topographical relief, and the color of overlapped fault plane represents the coseismic slip  
 93 distribution from Tung et al. (2016). The black lines mark the depth of faulting. The red lines represent active faults from Taylor and Yin (2009).

94 **2.2 Time series analysis**

95 The obtained daily time series reflects the surface motion due to the velocities, coseismic  
 96 displacements, postseismic parameters, seasonal terms (annual and semiannual), and non-  
 97 tectonic offsets primarily due to any changes in antennas and receivers. The component ( $\Delta N$ ,  $\Delta E$ ,  
 98  $\Delta U$ ) time series at discrete time epochs  $t_i$  can be modeled independently according to (Nikolaidis,  
 99 2002):

100 
$$y(t_i) = a + bt_i + c\sin(2\pi t_i) + d\cos(2\pi t_i) + e\sin(4\pi t_i) + f\cos(4\pi t_i) +$$
  
 101 
$$+ \sum_{j=1}^{n_g} g_j H(t_i - T_{g_j}) + \sum_{j=1}^{n_k} k_j \log\left(1 + \frac{t_i - T_{k_j}}{\tau_j}\right) H(t_i - T_{k_j}) + \varepsilon_{t_i} \quad (1)$$

102 The coefficient  $a$  is the value at the initial epoch  $t_0$ ,  $t_i$  denotes the time elapsed (in years)  
 103 from  $t_0$ , and the linear rate (slope)  $b$  represents the interseismic secular tectonic motion in mm/yr.  
 104 The coefficients  $c$ ,  $d$ ,  $e$ , and  $f$  denote annual and semi-annual variations. The seasonal variations in

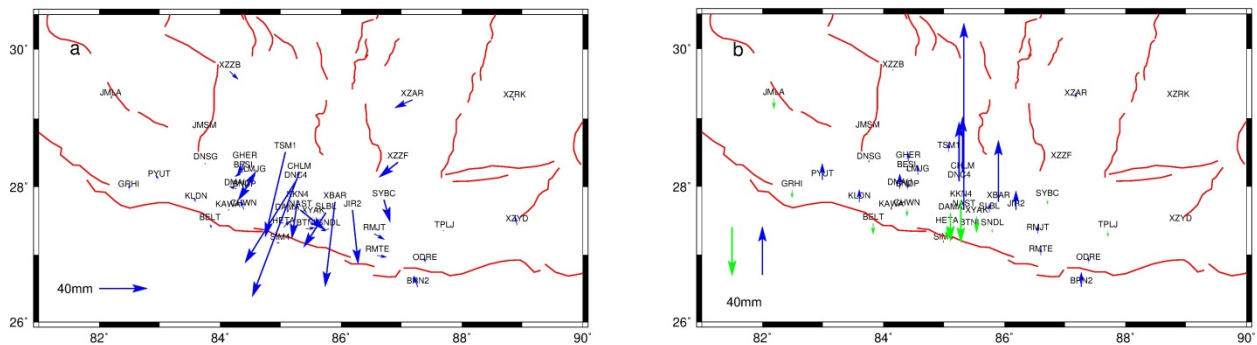
105 Himalayan range caused by the hydrological loading are up to 30-50 mm (Fu & Freymueller, 2012),  
106 and can bias the transient displacements, therefore the periodic terms need to be well dealt with.  
107 The magnitudes,  $g$ , of  $n_g$  jumps (offsets, steps, and discontinuities) are due to coseismic  
108 deformation and/or non-coseismic changes at epochs  $T_g$ .  $H$  denotes the discrete Heaviside  
109 function. With respect to the postseismic deformation term, it is often parameterized by  
110 exponential or logarithmic model, or combinations of both. The former is often associated with  
111 viscoelastic relaxation in the lower crust and the upper mantle (e.g., Shen et al., 1994; Nikolaidis,  
112 2002), while the latter is associated with afterslip within the extended rupture area (e.g., Savage  
113 and Svarc, 1997; Freed, et al., 2010 ). In this paper, we use the logarithmic parametrization, since  
114 related research showed that the afterslip mechanism dominated the Gorkha earthquake  
115 (Gualandi et al., 2016; Mencin et al., 2016; Sreejith et al., 2016; Zhao et al., 2017; Wang & Fialko,  
116 2018; Jiang et al., 2019). The postseismic term includes the amplitudes  $k_j$ , postseismic events  
117 starting at epochs  $T_k$  and a decaying constant  $\tau_j$ , which characterizes how fast the postseismic  
118 deformation decays with time. The noise term  $\varepsilon_i$  is considered as the sum of errors and  
119 unmodeled residuals.

120 Fitting the time series, we can clearly extract the various motions, in particular, the  
121 postseismic deformation. For the sake of reliability and obtaining the postseismic parameters with  
122 a high signal-to-noise ratio, two more steps were taken: Firstly, we estimated secular velocities of  
123 sites which operated for more than 2 years before the earthquake, and combined those with GPS  
124 velocities provided by Ader et al. (2012) and Bettinelli et al. (2006), through seven parameter  
125 transformations to obtain the integrated velocity field in the ITRF2014 reference frame. We then  
126 interpolated the velocities using the VISR software (Shen et al., 2015), and re-estimated the time  
127 series parameter (equation 1), constraining the prior secular velocities. Secondly, motivated by the  
128 work of Savage & Svarc (2009) and Barbot et al. (2009), we employed the principal component  
129 analysis (PCA) to extract a common postseismic signal for all the displacement time series and  
130 their principal components (Fig. S2). The first principal component clearly represented the  
131 postseismic process. On account of the non-linearity of the postseismic deformation model  
132 parameter  $\tau$ , we used trial-and-error over a range of decay values to minimize the sum of the  
133 squared residuals between the observations and model. We then fit each coordinate time series

134 (equation 1) with the optimal  $\tau$ , and finally extracted the postseismic parameter for each site (Fig.  
135 S3).

### 136 2.3 Postseismic deformation

137 The 4.8-year cumulative postseismic displacements (Fig. 2) associated with the 2015 Gorkha  
138 earthquake exhibit similar patterns as the coseismic offsets (Elliott et al., 2016; Gualandi et al.,  
139 2016; Mencin et al., 2016). Most GPS sites continue to move southward after the earthquake,  
140 showing a dominant thrust feature with minor dextral strike-slip motion along southeast Nepal. As  
141 the earthquake ruptured toward the southeast, significant postseismic displacements are primarily  
142 distributed across the High Himalaya region. The largest postseismic displacement at site CHLM  
143 reaches up to -93.84 mm, -31.87 mm and 36.64 mm for the N, E, U directions, respectively.  
144 Displacements in the north of the rupture area are much larger compared to displacements south  
145 of the rupture, which has been confirmed by many studies (Zhao et al., 2017; Wang & Fialko, 2018;  
146 Jiang et al., 2018; Jiang et al., 2019; Jouanne et al., 2019; Tian et al., 2020), implying the possible  
147 existence of afterslip downdip of coseismic rupture. In the vertical direction, most sites  
148 experienced ongoing uplift after the Gorkha earthquake, while some sites to the south of the  
149 rupture area subsided. The extremely large uplift of site NAST is not reliable, since it suffered from  
150 rapid subsidence prior to the mainshock (Zhao et al., 2017). Therefore, we exclude the vertical  
151 component of site NAST in modeling the fault slip.



152 **Fig. 2** The cumulative horizontal (a) and vertical (b) postseismic displacements exacted from GPS displacement time series. The red  
153 lines represent active faults.

## 154 3. Method of Modeling postseismic deformation

### 155 3.1 Finite element model

156 The superiority of Finite element models (FEMs) in simulating the elastic dislocation and the

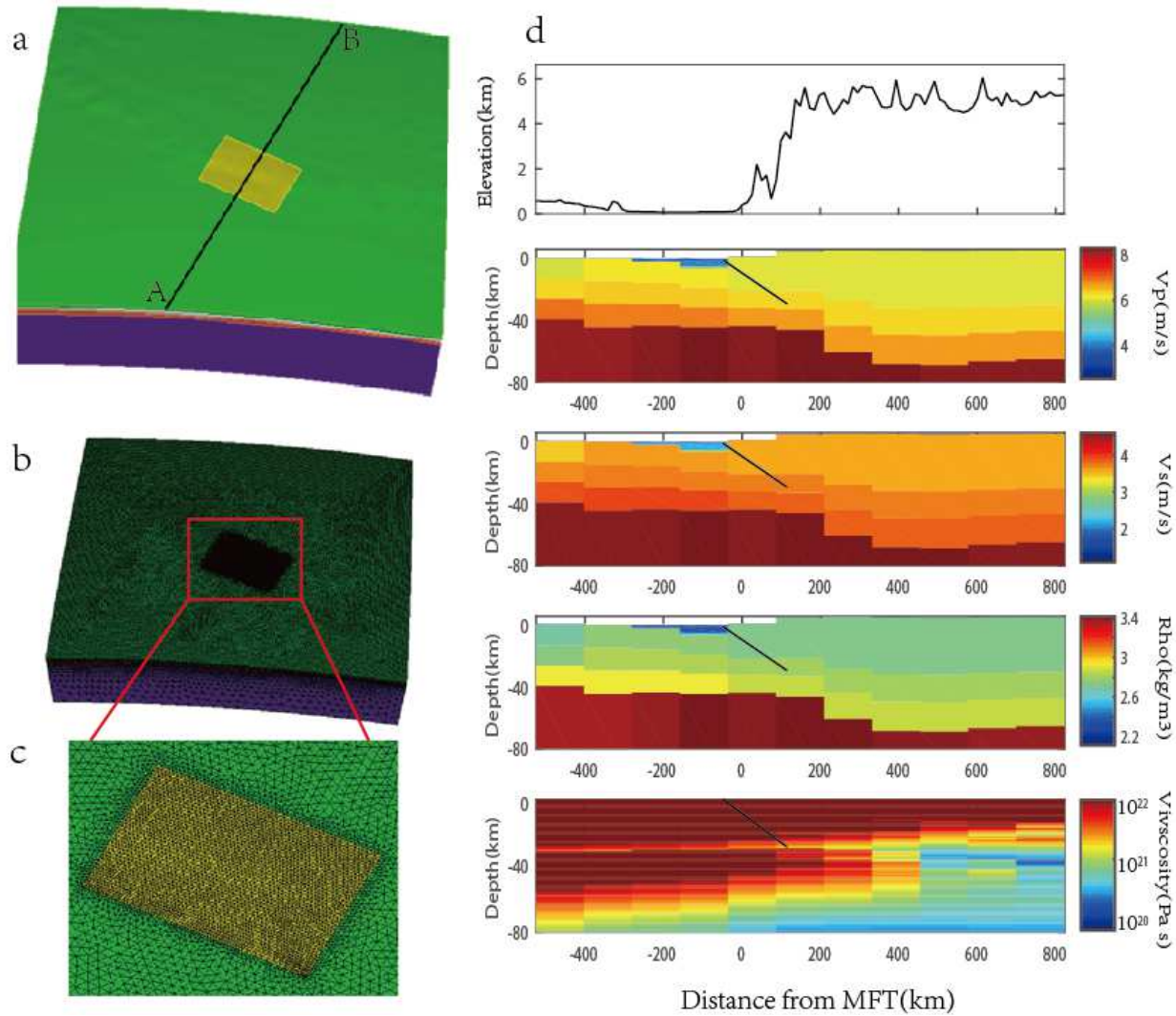
157 viscoelastic relaxation with heterogeneous material properties has been proven by previous  
158 studies (Masterlark et al., 2012; Hughes et al., 2010; Hines et al., 2016; Hsu et al., 2014; Tung et al.,  
159 2016; Pratama et al., 2017). In the view of the strong topographical fluctuations and heterogeneity  
160 across the Himalayan region, the spherical FEM with topography and heterogeneity was  
161 constructed using the CUBIT software (Blacker et al., 2016).

162 We defined a spherical shell from the mantle to the surface shaped by the irregular  
163 topographical geometry in the target region (Fig. 3) with a resolution of about 1 km obtained from  
164 the SRTM30 software (Becker et al., 2009). The 3D FEM extended over 78–92°E and 23–34°N, from  
165 the ground surface to a depth of 300 km, incorporating the upper crust, the middle crust, The  
166 lower crust and the upper mantle, and the layer interfaces were interpolated based on CRUST 1.0  
167 (Laske, 2013). The heterogeneous elastic material properties were characterized by spatially  
168 variable P and S wave velocities, and the density based on CRUST 1.0 (Laske, 2013). A spatially  
169 variable fully anisotropic viscous model was assigned (Fig. S4), based on Sun et al. (2013).  
170 Furthermore, we assumed zero displacements as side and bottom boundary conditions to take  
171 into account their very large extent, along with the stress-free top surface.

172 The 3D FEM spanned about 1400 km, 1200 km and 300 km in length, width and depth. The  
173 blocks were meshed and discretized by 186,079 tetrahedral elements. The elements in the upper  
174 crust were of a length of about 11 km, while the element size increased up to a factor of 5 at the  
175 deeper depth in the mantle for the sake of computational time saving; the elements near the fault  
176 were dense with a length of about 5 km to capture strong variable deformation. Because the FEM  
177 configuration used by Tung et al. (2016) was basically matched ours, we adopted the same refined  
178 coseismic rupture to drive viscoelastic relaxation. On the basis of that, we assigned the same fault  
179 geometry with a planar patch centered at (27.95°N, 85.27°E) with a dip and strike of 10° and 294°  
180 (Tung et al., 2016), and, additionally, extended the fault to the spatial scale of 286km × 200km  
181 (length × width) for the inversion of afterslip.

182 We performed the calculation with the finite element software PYLITH (Aagaard et al., 2013),  
183 which was widely applied to postseismic deformation modelling (Hines et al., 2016; Pratama et al.,  
184 2017) and to generate the Green's function (Diao et al., 2013; Hsu et al., 2014; Hines et al., 2016).

185



186  
 187 **Fig. 3** FEM structure used in the numerical simulation. (a) The yellow rectangle denotes fault rupture. The top surface exhibits  
 188 topographical relief. The color blocks denote the upper, middle and lower crust and the mantle, respectively. The profile AB is  
 189 normal to the MFT. (b) Map view of the FEM mesh. (c) The larger view of the FEM mesh in the near-field area of the Gorkha  
 190 earthquake. (d) The elevation,  $V_p$ ,  $V_s$ , density and viscosity variations along the profile AB. The black line is the source rupture  
 191 plane.

192 **3.2 Viscoelastic relaxation**

193 Viscoelastic relaxation due to the coseismic stress changes in the lower crust and upper  
 194 mantle can explain the postseismic deformation at extensive spatial scales (Freed et al., 2004,  
 195 2007; Huang et al., 2014; Rousset et al., 2012). The previous studies calculated the viscoelastic  
 196 relaxation based on the lateral heterogeneous or layered model, and evaluated viscoelastic  
 197 relaxation in the postseismic process after the Gorkha earthquake (Zhao et al., 2017; Wang &  
 198 Fialko, 2017; Jiang et al., 2018; Jouanne et al., 2019; Tian et al., 2020; Liu et al., 2020). Differing  
 199 from these models, we designated spatial variable viscosities to account for the heterogeneous

200 rheological properties across the Himalayan region. Furthermore, we simulated the viscoelastic  
201 relaxation with the refined rupture model of Tung et al. (2016), which was inverted by a 3D  
202 heterogeneous FEM with input from GPS and INSAR data consistent with other published models  
203 (Sreejith et al., 2016; Wang & Fialko, 2018),

### 204 **3.3 Afterslip**

205 The sudden coseismic deformation triggers the aseismic slip on the extended coseismic  
206 rupture area (Marone, 1991; Perfettini et al., 2004; Hsu et al., 2006; Barbot et al., 2009). The  
207 afterslip plays an important role in the postseismic process from several days to several months  
208 (Barbot et al., 2008; Segall, 2010; Huang et al., 2014). In order to investigate the distribution of  
209 afterslip following the Gorkha earthquake, we also performed a 3D FEM inversion using the cGPS  
210 data as input. The fault, 286 km long and 200 km wide, was discretized by a grid of 28×20 into 560  
211 subfault patches with a dimension of 10.21 ×10 km, and with Green's functions for each subfault  
212 patch due to a unit slip along dip and strike.

213 With the generated Green's functions, we assumed that the afterslip can be described by a  
214 dislocation model of distributed slip. The objective function is:

$$215 \quad F = ||W(Gm-d)|| + \beta ||\nabla^2 m||$$

216 The first term represents the misfit between modeled and observed displacements, Where W is  
217 the weight matrix inferred from observation uncertainties, G is the Green's functions, m is the  
218 estimated slip distribution, and d is the observations. The second term is Laplacian smoothing to  
219 avoid abrupt slip variation, where  $\beta$  is smoothness and  $\nabla^2$  is the Laplacian operator.

220 An algorithm was then developed to invert the smoothed afterslip distribution achieved by a  
221 constrained least-squares optimization based on the steepest descent method, motivated by Wang  
222 et al. (2013). The optimal smoothness was determined by the trade-off between the roughness  
223 and data misfit.

## 224 **4. Results**

### 225 **4.1 Verification of 3D Finite element model and methodology**

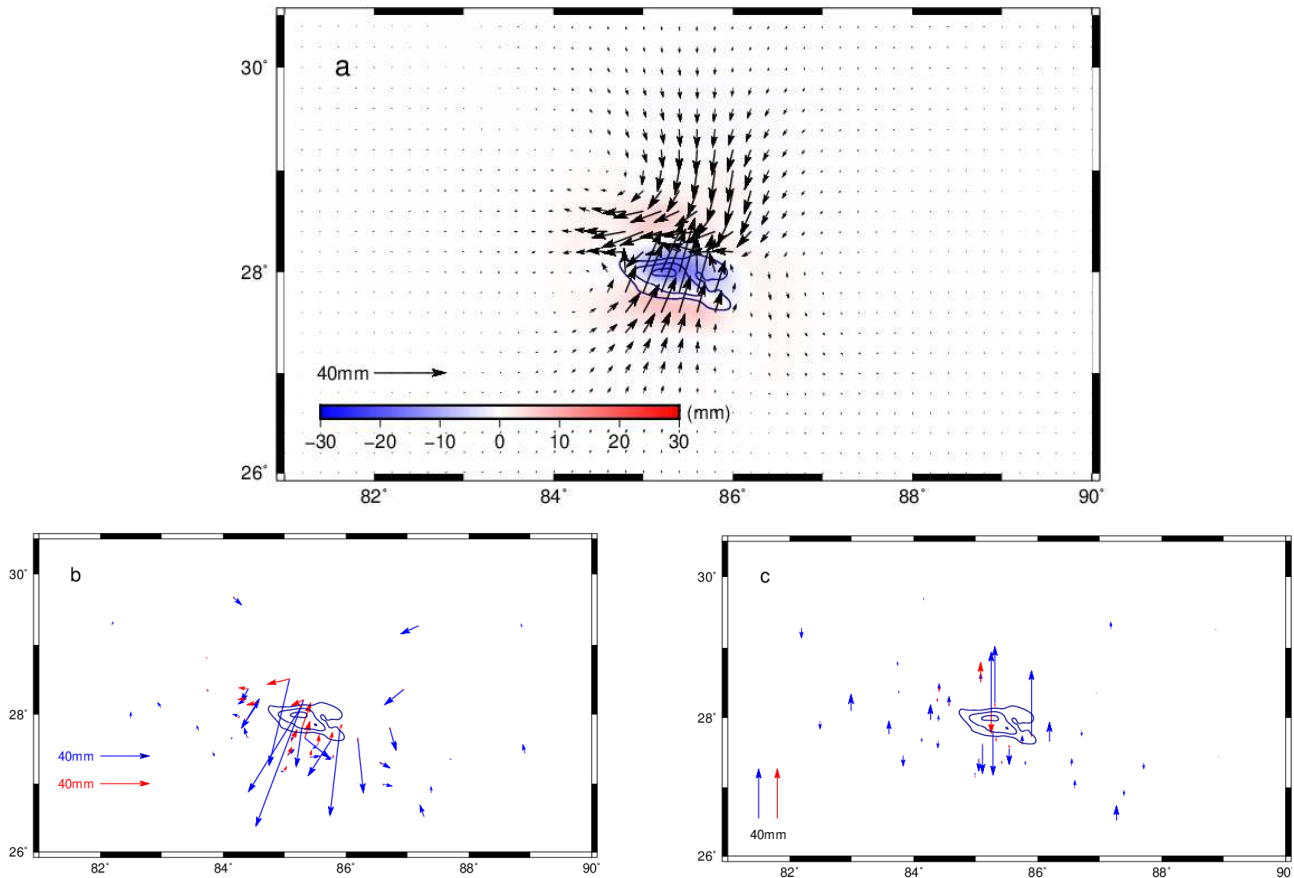
226 In order to validate our FEM calculations, we tested a flat layered model with elastic upper  
227 and middle crust overlaying a viscoelastic lower crust and mantle, and assigned viscosity values of  
228  $1.6 \times 10^{19} \text{ Pa} \cdot \text{s}$  for the lower crust and  $10^{20} \text{ Pa} \cdot \text{s}$  for the mantle according to Jiang et al. (2018).

229 Comparing the afterslip and viscoelastic relaxation predicted by our FEM with afterslip by the SDM  
230 software (Wang et al., 2013) and viscoelastic relaxation by the PSGRN/PSCMP software (Wang et  
231 al., 2006), respectively (Fig. S5 and S6), we find coherent patterns and equivalent magnitudes of  
232 afterslip and viscoelastic relaxation.

#### 233 **4.2 Viscoelastic relaxation**

234 We characterized the viscoelastic material as the bi-viscoelastic Burgers model, incorporating  
235 a transient relaxing Kelvin element in series with a steady-state Maxwell element. For simplicity,  
236 we set a constant ratio of 0.1 between Kelvin and Maxwell viscosities (Hu et al., 2016; Hines et al.,  
237 2016; Zhao et al., 2017). The viscoelastic relaxation by the forward model exhibits two quadrants  
238 of horizontal displacements, namely, pronounced northward motion in the south of the rupture  
239 and southward motion in the north. The directions of the predicted viscoelastic relaxation in the  
240 south of the rupture area are opposite to the observations. In the vertical direction, there is  
241 obvious subsidence in the near field and uplift in the surrounding areas (Fig. 4). The relatively  
242 small horizontal and vertical displacements over 4.8 years after Gorkha earthquake imply that  
243 viscoelastic relaxation is not indicative of the postseismic process.

244 We additionally characterized the rheological property as a Maxwell body, and obtained even  
245 less significant viscoelastic relaxation (Fig. S7). Lacking a Kelvin element, Maxwell rheology usually  
246 produces smaller viscoelastic relaxation than a Burgers rheology. In the horizontal component, the  
247 Maxwell rheology indicates a similar pattern to that of the Burgers rheology. In the vertical  
248 direction, there is subsidence in the rupture area for both models, but insignificant uplift to the  
249 south of rupture area.

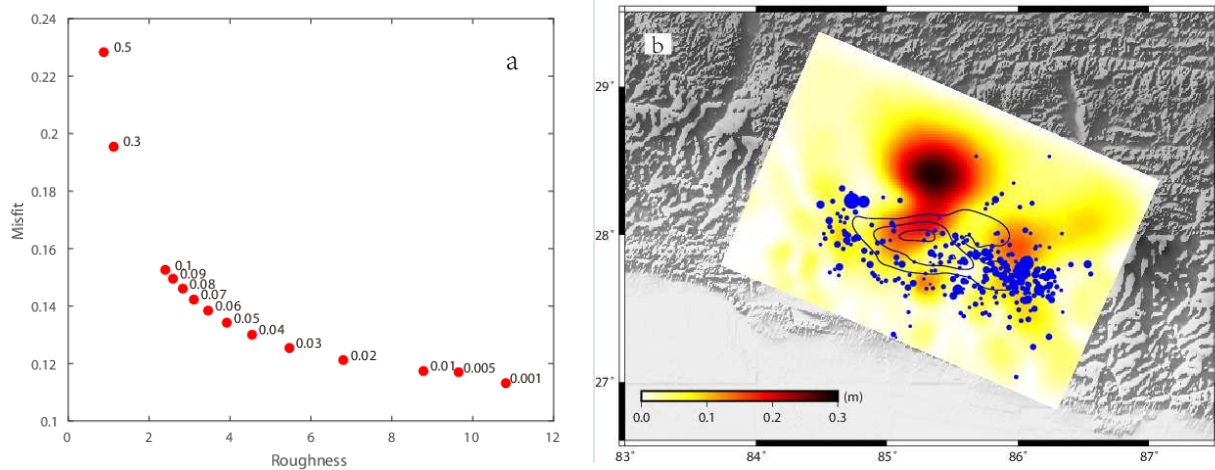


250 **Fig. 4** The predicted postseismic displacements due to a bi-viscoelastic Burgers model. (a) The color scale represents the vertical  
 251 component, and the black arrows represent the horizontal component. (b) The comparison between the predicted viscoelastic  
 252 relaxation (red arrows) and observations (blue arrows) in the horizontal component and (c) the vertical component. The dark blue  
 253 contours denote the coseismic slip distribution on the fault.  
 254

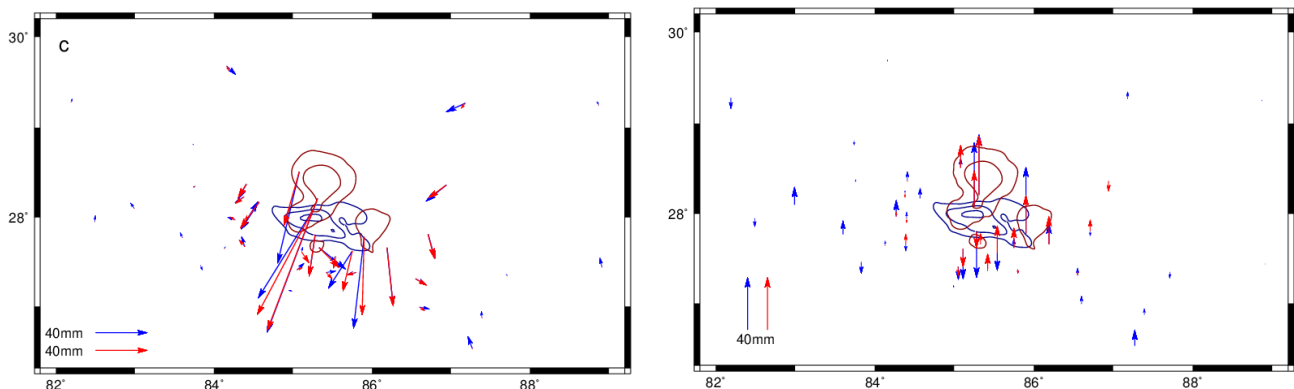
### 255 4.3 Afterslip

256 Next, we modeled the postseismic deformation by afterslip on the fault interface. The knee  
 257 of the tradeoff curve between the model roughness and data misfit was selected as the optimal  
 258 smoothing factor (Fig. 5); a smoothing factor of  $\beta = 0.06$  was chosen in our final solution. With  
 259 viscoelastic relaxation deducted, the observed horizontal surface displacements are well explained  
 260 by the downdip afterslip model (Fig. 6). The postseismic displacements due to afterslip are much  
 261 larger than those associated with viscoelastic relaxation, suggesting that the afterslip plays the  
 262 dominant role in the postseismic process during the first 4.8 years after the event. The afterslip is  
 263 mainly distributed downdip of the coseismic rupture, which would be responsible for the much  
 264 larger postseismic deformation north of the rupture than south of the rupture. The high-slip patch  
 265 is located at the depth of about 25-30 km with a peak of 0.28 m. Afterslip occurs at the periphery

266 of the coseismic rupture, in the areas characterized by low aftershock activity (Barbot et al., 2009).  
 267 The moment release by postseismic afterslip is  $7.32 \times 10^{19}$  N m, equivalent to a moment  
 268 magnitude of  $M_w \sim 7.18$ , approximately 6.7% of the mainshock moment release of  $1.09 \times 10^{21}$   
 269 Nm of the coseismic moment release (Tung et al., 2016).



270 **Fig. 5** (a) Trade-off curve between model roughness and misfit. Numbers indicate the smoothing factor  $\beta$ . (b) The inverted afterslip  
 271 distribution. The color scale denotes the inverted afterslip distribution. The black contours denote the coseismic slip distribution on the fault.  
 272 The blue circles denote the aftershocks after the Gorkha earthquake, and the size indicates the magnitude.



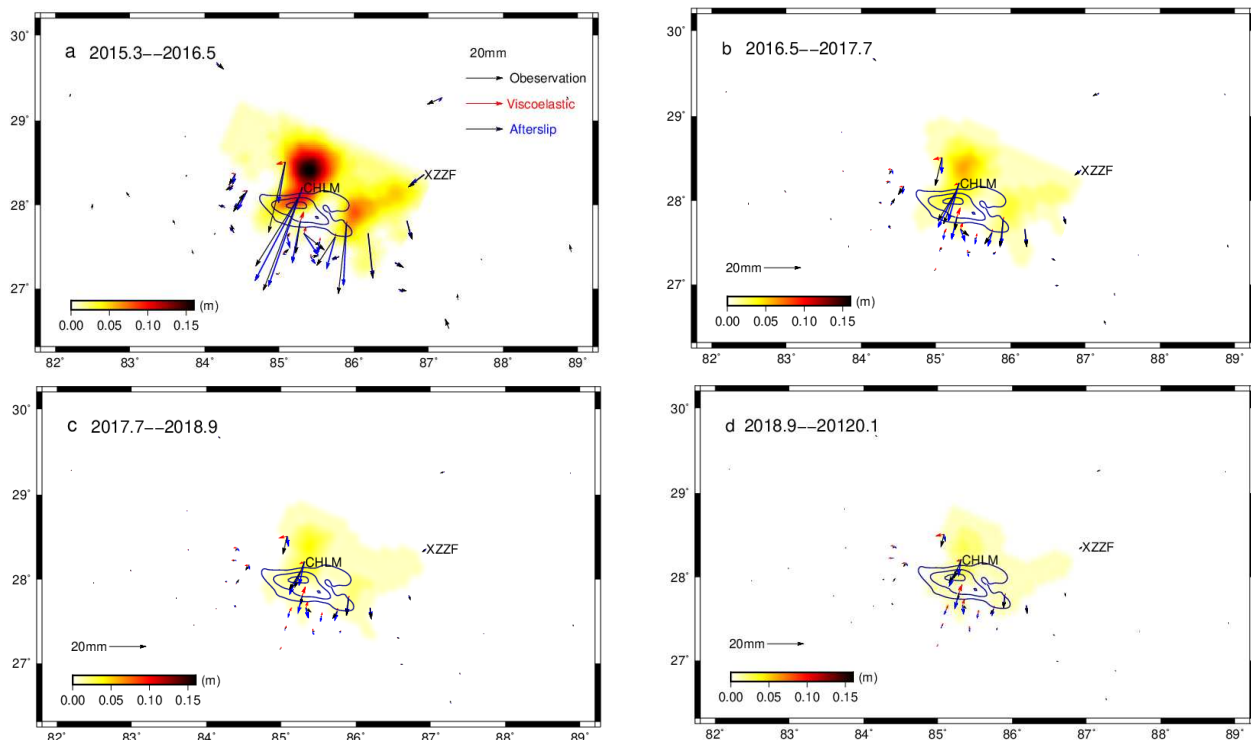
273 **Fig. 6** The observed postseismic displacement (blue arrows) and predicted postseismic displacement (red arrows) due to afterslip.  
 274 The dark blue and dark red contours denote the coseismic slip and afterslip distribution on the fault.

275 To examine whether the afterslip is well constrained by the GPS data, we conducted a  
 276 checkerboard test for the resolution (Fig. S8). The slip model merged  $4 \times 4$  subpatches into a single  
 277 pixel to exhibit  $7 \times 5$  checkered asperities (each pixel of  $40.85 \times 40$  km) of 0 and 1.4 m slip. We then  
 278 compared the checkerboard pattern slip with the slip model inverted by GPS displacements, and  
 279 found that slip distribution to be well recovered in spite of minimal distortion and discernible  
 280 artifacts along the down edge of the slipping patches. The far downdip of the fault was not well  
 281 constrained compared to the shallower part of fault, which can be explained by the sparse

282 clustered GPS sites in South Tibet. A joint inversion of GPS and InSAR and/or more GPS sites  
283 distribution deployed in South Tibet should provide a better resolution.

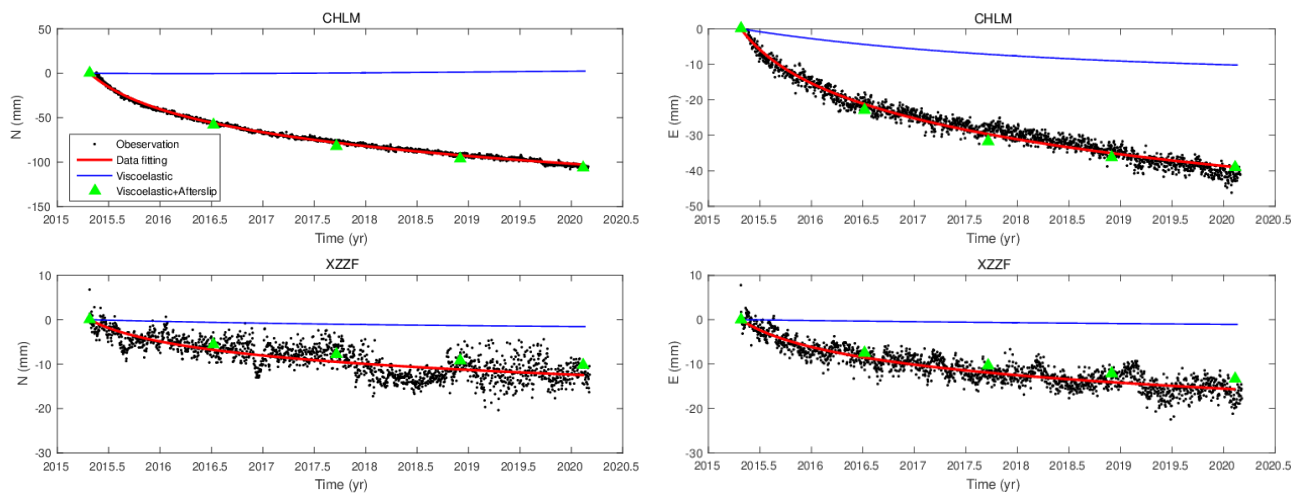
#### 284 4.4 Temporal evolution of the deformation and its mechanisms

285 We divided the postseismic deformation over 4.8 years after the Gorkha earthquake into four  
286 equal time periods of 1.2 years (Fig. 7). The overall patterns of observed postseismic deformation,  
287 including both afterslip and postseismic relaxation, during the four time periods are similar: most  
288 sites moved southwards, similar to the coseismic displacements. The magnitude of postseismic  
289 deformation decays rapidly; the deformation occurring in the first 1.2 years decreases rapidly and  
290 averages to about 53.6% of the entire postseismic signal (maximum slip of 0.16 m), the second  
291 interval to about 22.2% (0.06 m), the third to about 13.9% (0.04m) and about 10.2% (0.03 m) in  
292 the last 1.2 years. Snapshots of the spatial distribution due to afterslip alone indicate that most of  
293 it occurs downdip of the coseismic rupture. The viscoelastic relaxation component shows a similar  
294 pattern but smaller slip magnitudes. The afterslip downdip of the coseismic rupture is usually  
295 associated with velocity-strengthening behavior, results in enduring aseismic slip following the  
296 earthquake (Lienkaemper & McFarland, 2017; Tian et al., 2020).



297 **Fig. 7** Comparisons of observed and calculated displacements, including contributions from viscoelastic relaxation and afterslip  
298 during the different periods. Horizontal displacements are presented by arrows. The color inset in each panel shows horizontal  
299 residuals. The dark blue contours denote the coseismic slip distribution on the fault.

300 Fig. 8 shows how the postseismic deformation evolves with time and the individual  
 301 contributions of afterslip and viscoelastic relaxation. At the site CHLM, the predicted viscoelastic  
 302 relaxation is opposite to the observation for the N component. For the E component, the  
 303 contribution rates of viscoelastic relaxation to postseismic deformation at site CHLM during four  
 304 different time periods are 19.2%, 22.7%, 24.8%, and 26.2%, respectively. At the site XZZF in the  
 305 Tibet, the contribution rates of viscoelastic relaxation to postseismic deformation during four  
 306 different time periods are 10.5%, 12.5%, 13.7%, and 14.5% for the N component, and 4.4%, 6.0%,  
 307 7.1% and 8.0% for the E component. The viscoelastic relaxation plays insignificant role in the  
 308 postseismic process over the 4.8 years after Gorkha earthquake, but its contribution to the  
 309 postseismic deformation gradually increases slightly. Longer spans of GPS displacements after the  
 310 Gorkha earthquake show that postseismic slip is still ongoing.



311 **Fig. 8** The postseismic deformation daily displacement time series of the north and east components at GPS sites CHLM and XZZF.  
 312 Black dots indicate the observed displacements. The red line indicates the data fitting of the postseismic deformation (Equation 1).  
 313 The blue line indicates the predicted viscoelastic relaxation. The green triangles indicate the sum of predicted viscoelastic  
 314 relaxation and the postseismic deformation due to afterslip.

315

## 316 5. Discussion

### 317 5.1 Effect of heterogeneity under Tibet

318 In the context of crustal rheology, evidence from seismic receiver functions, geodetic  
 319 inversion, resistivity and temperature profiles across the whole Tibetan Plateau show lateral  
 320 heterogeneous properties (Cattin et al., 2001; Hetényi et al., 2006; Bai et al., 2010; Huang et al.,  
 321 2014; Avouac et al., 2015; Sun et al., 2013). The assumption of lateral uniform viscosity hardly

322 represents the spatially-variable viscous properties from the Tibetan plate to the Indian plate, and  
323 may inaccurately estimate the extent and magnitude of viscoelastic relaxation in the Himalayan  
324 region. Compared with viscoelastic relaxation of our model with that of the flat layered model  
325 (Jiang et al., 2018) (Fig. S5), we find that the softer viscous lower crust over the entire region  
326 inevitably brings about an excessive estimation of viscous relaxation in Nepal. The –simple  
327 heterogeneous rheological models (Zhao et al., 2017; Wang & Fialko, 2018; Tian et al., 2020),  
328 incorporates the viscous lower crust layer under Tibetan plate. To investigate the difference  
329 between a fully heterogeneous model and the simple heterogeneous model, we calculated the  
330 viscoelastic relaxation with the software VISCO2.5D (Pollitz, 2014), following the simple  
331 heterogeneous rheological structure and effective viscosities inferred by Zhao et al. (2017). The  
332 viscoelastic relaxation of the simple heterogeneous model exhibits a two quadrant pattern,  
333 northward motion in the south of the rupture, southward motion in the north of the rupture, and  
334 uplift in the north and subsidence in the south (Fig. S9). The opposite sign of the predicted  
335 displacements with the observations in the south of the rupture area is consistent with our 3D  
336 FEM model, consistent with other studies (Wang & Fialko et al., 2018; Jiang et al., 2018). However,  
337 it is different from the southward motion predicted by the Tian et al. (2020). Their lower viscosity  
338 of the lower crust and mantle under the Tibetan plate with the simple heterogeneous model,  
339 results in the larger postseismic displacements in Tibet than our model. Additionally, the distance  
340 of the transition zone from the MFT is chosen as 167 km, further than the model of Sun et al.,  
341 (2013), leading to the smaller magnitude of the postseismic deformation in the south of the  
342 rupture area. It is difficult to explain the postseismic deformation, occurring both in Nepal and  
343 Tibet, by viscous relaxation.

344 The lower viscosity of the lower crust and mantle under the Tibetan plateau could account for  
345 the postseismic displacements in Tibet, but it leads to a larger discrepancy in the south of the  
346 rupture area. The opposite signs between observations and model predictions in the south of the  
347 rupture area could be reduced by assuming that a transition from strong to weak lower crust  
348 occurs farther to the north (Wang & Fialko, 2018). However, this would be inconsistent with the  
349 assumption that the topographic slopes are controlled by the viscosity of material in the  
350 underlying lower crust (Clark & Royden, 2000; Royden et al., 1997).

351 The postseismic viscoelastic relaxation obtained from geodetic measurements sheds some  
352 light on the rheology structure of Himalayan region. Wang & Fialko (2018) and Jiang et al. (2018)  
353 inferred  $>10^{18}$  Pa · s and  $1.6 \times 10^{19}$  Pa · s for the lower crust beneath the Tibet. Zhao et al. (2017)  
354 and Tian et al. (2020), respectively, inferred a transient viscosity of  $8 \times 10^{18}$  and  $5 \times 10^{17}$  Pa · s, a  
355 steady viscosity of  $8 \times 10^{19}$  and  $5 \times 10^{18}$  Pa · s for this layer. Liu et al. (2020) deduced that the  
356 effective viscosity would decrease northward from  $10^{18}$  -  $10^{19}$  Pa · s around the rupture zone to  $\sim 3$   
357  $\times 10^{16}$  -  $10^{18}$  Pa · s  $\sim 150$  km north. Similar studies were conducted for several earthquakes around  
358 Tibetan Plateau. The effective viscosities on the order of magnitude of  $10^{18}$ -  $10^{19}$  Pa · s was  
359 predicted in studies of the 2001 Mw7.8 Kokoxili earthquake (Ryder et al., 2011; Wen et al., 2012),  
360 2005 Mw7.6 Kashmir earthquake (Wang & Fialko, 2014) and 2008 Mw7.9 Wenchuan earthquake  
361 (Huang et al., 2014). The above studies, constraining effective viscosities by geodetic postseismic  
362 deformation, ignored the dynamic propagating stress changes from viscoelastic relaxation and  
363 those induced by any afterslip, and may somewhat estimate lower effective postseismic viscosities  
364 (Liu et al., 2020). Strain rates were highest just after the earthquakes, and the effective viscosity  
365 were equivalently lower (Liu et al., 2020). The time span is another factor which influences the  
366 inferred value of the viscosity. The rheological structure used in this paper, inferred from seismic  
367 velocities and GPS velocities, represents the long-term and steady state viscosity, which is larger  
368 than the studies above.

## 369 **5.2 Comparison with the previous afterslip models**

370 The afterslip associated with the Gorkha earthquake is broadly investigated by several studies  
371 based on the GPS and/or InSAR data (Gualandi et al., 2016; Mencin et al., 2016; Sreejith et al.,  
372 2016; Zhao et al., 2017; Wang & Fialko, 2018; Jiang et al., 2018; Jiang et al., 2019; Tian et al., 2020).  
373 These studies have found similar afterslip patterns as our study; afterslip mainly occurs downdip  
374 of the rupture area. The high afterslip patch constrained by the joint inversion of GPS and InSAR  
375 (Wang & Fialko, 2017; Sreejith et al., 2016) data is more easterly than the high afterslip patch  
376 constrained by GPS alone, which might be due to the lack of GPS sites in the north of the rupture  
377 area. The moment released by afterslip is about  $7.32 \times 10^{19}$  Nm over first 4.8 years, which is  
378 echoed by  $5.5 \times 10^{19}$  Nm over first 1 year (Zhao et al., 2017),  $1.2 \times 10^{20}$  Nm over first 1.6  
379 years (Jiang et al., 2018),  $6.0 \times 10^{19}$  Nm and  $1.2 \times 10^{20}$  Nm over first 2 years (Wang & Fialko, 2018);

380 Jiang et al.,2019), and a moment between  $1.21 \times 10^{20}$  Nm and  $2.37 \times 10^{20}$  Nm over 1.16 years (Liu  
381 et al.,2020) .The low moment release due to afterslip, approximating 6.7% of the mainshock  
382 moment release, is also found for several earthquakes where afterslip occurred downdip of the  
383 rupture (Hsu et al., 2006; Ryder et al., 2011; Huang et al., 2014; Lienkaemper & McFarland, 2017).

384 Different from the previous studies, we inverted the afterslip based on the heterogeneous  
385 elastic model including the topographic relief and a spherical shell. We compared the afterslip  
386 inverted by 3D FEM and flat layered models, and found the WRMS misfit between the afterslip  
387 and observations to be 3.18 mm for the FEM and 3.19 mm for the flat layered mode. The afterslip  
388 distribution of the flat layered model is somewhat smaller from that of the 3D FEM. The high value  
389 patch of afterslip inverted by flat layered model is more concentrated and maximum afterslip is up  
390 to 0.31 m (Fig. S10), larger than the 0.28 m of the FEM. However, the moment released by  
391 afterslip of the flat layered model is equivalent to Mw7.15, lower than Mw7.18 of the 3D FEM.

### 392 **5.3 The potential poroelastic rebound**

393 When an earthquake occurs, sudden pore fluid pressure changes in the ambient rocks  
394 accompanies with the coseismic pressure changes, and then gradually evolves towards an  
395 equilibrium condition as the flow of fluid is restored, leading to time-dependent surface  
396 deformation (Peltzer et al., 1998; Wang & Kümpel, 2003). It is difficult to solve the problem  
397 analytically because the deformation and pore pressure fields are coupled through the equilibrium  
398 and diffusion equation (Segall, 2010). The characteristics of anisotropic rocks further complicate  
399 the calculation. One common way is to calculate postseismic poroelastic rebound through  
400 differencing coseismic deformation models under the undrained and drained conditions,  
401 represented by variable Poisson's ratios (Fialko et al., 2004; Barbot et al., 2010; Wang & Fialko,  
402 2018; Gonzalez-Ortega et al., 2014; Hughes et al.,2010; Hu et al., 2014). We approximately  
403 evaluated the potential poroelastic rebound without considering the time-dependent process and  
404 any heterogeneity. The poroelastic layer was assumed to be within the top 20 km of upper crust,  
405 while the undrained and drained Poisson's ratios were set to 0.28 and 0.25, respectively, and the  
406 rupture model of Tung et al. (2016) was used to drive the poroelastic rebound. Our results show  
407 that the poroelastic rebound (Fig. S11) spreads out from the rupture area; large poroelastic  
408 rebound concentrates the rupture area. However, the maximum displacement is on the order of

409 millimeter, far less than the effects of afterslip and postseismic relaxation, which echoes previous  
410 studies (Zhao et al., 2017; Wang & Fialko, 2018).

#### 411 **5.4 Insight into the seismic risk**

412 Due to the rapid plate convergence of Indian-Eurasian collision and high strain accumulation,  
413 the Himalayan collision zone is prone to frequent devastating earthquakes. During the interseismic  
414 period, the MHT is locked from the surface to a distance of approximately 100 km downdip,  
415 corresponding to a depth of 15 to 20 km based on long time geodetic measurements (Ader et al.,  
416 2012; Stevens & Avouac, 2015; Liu et al., 2016). The background seismicity along the Himalayan  
417 arc is clustered along a relatively narrow zone, which approximately coincides with the downdip  
418 end of the locked fault zone (Cattin & Avouac, 2000; Bollinger et al., 2004) and the zone of  
419 greatest shear stress accumulation (Ader et al.,2012). More detailed inversions for distributed  
420 interseismic coupling find that the MHT appears nearly fully locked to the south of the front of the  
421 Higher Himalaya and fully creeping to the north of it. The transition from unstable to stable slip  
422 behavior can be related to the temperature at depth (Ader et al., 2012; Stevens & Avouac, 2015).

423 The Gorkha earthquake ruptured the deep part of the fully locked segment of the MHT  
424 (Avouac et al., 2015; Galetzka et al., 2015; Gualandi et al.,2016; Elliott et al., 2016; Qiu et al., 2016),  
425 only releasing a small amount of seismic moment deficit (Feng et al., 2015; Liu et al.,2019); the  
426 inferred afterslip was concentrated at the deeper extent of the coseismic rupture, followed two  
427 weeks later by the Mw7.3 aftershock, which unzipped the eastern edge of the mainshock (Zhang  
428 et al.,2015; Wang & Fialko, 2018), leaving the shallow portion and the west of the mainshock  
429 rupture areas still locked. Considering the interseismic fault coupling and the small amount of  
430 energy released during the coseismic and postseismic periods, the unzipped shallow portion and  
431 western segment of the MHT are still at the high seismic risk (Mencin et al., 2016; Elliott et al.,  
432 2016; Zhao et al.,2017; Wang & Fialko, 2018; Tian et al.,2020; Liu et al.,2020).

#### 433 **6. Conclusion**

434 We processed GPS displacement time series of 39 sites in Nepal and South Tibet of China,  
435 applying PCA and prior velocity constraints to extract postseismic displacements over 4.8 years  
436 after the 2015 Gorkha earthquake. The postseismic displacements show the southward and  
437 upward motion around the epicentral area. We then constructed the 3D FEM to explicitly account

438 for the surface topography, earth curvature and heterogeneous material properties to refine the  
439 postseismic deformation after the earthquake. With the more realistic FEM, the Burgers rheology  
440 generates the viscoelastic relaxation on the order of a centimeter. The viscoelastic relaxation  
441 shows the southward motion in the north of the rupture, but nearly exhibits the opposite  
442 direction to the observations in the south of the rupture. However, the observed postseismic  
443 motions for this earthquake are dominated by afterslip. The inverted afterslip is mainly distributed  
444 downdip of the coseismic rupture with a peak of  $\sim 28$  cm, in the area characterized by low  
445 aftershock activities. The moment release by afterslip is  $7.32 \times 10^{19}$  N m, equivalent to a moment  
446 magnitude  $M_w \sim 7.18$ , approximately 6.7% of the mainshock moment release. Considering the  
447 accumulated moment deficit and the small amount energy release during and after the 2015  
448 Gorkha earthquake, the lack of slip on a shallow portion and western segment of the MHT implies  
449 continued seismic hazard into the future.

#### 450 **Abbreviations**

451 FEM: Finite Element Model; MFT: Main Frontal Thrust; MHT: Main Himalayan Thrust; cGPS: continuous GPS; NGL: Nevada Geodetic  
452 Laboratory; CMONOC: Crustal Movement Observation Network of China; PCA: Principal Component Analysis;

#### 453 **Availability of data and materials**

454 The datasets used and/or analyzed during the current study are available from the corresponding author on reasonable request.  
455 GPS data in Nepal are provided by UNAVCO. Time series of the Nepal station positions are provided by Nevada Geodetic Laboratory.  
456 GPS data in South Tibet are from the Crustal Movement Observation Network of China

#### 457 **Funding**

458 This work was supported by National Science Foundation of China (41490615),  
459 Special Research Project for Earthquake Science of China (2015419024) and the Spark Program of Earthquake Technology of CEA  
460 (XH20056Y).

#### 461 **Contributions**

462 LS and WG designed the research. LS, XS and FS calculated and analyzed the data. LS wrote the software. JY plotted the figures. LS  
463 wrote the manuscript with support from WG. All authors read and approved the final manuscript.

#### 464 **Competing interests**

465 The authors declare that they have no competing interest.

#### 466 **Acknowledgements**

467 We thank David Mencin for assisting us in the data download. We thank Cecep Pratama, Charles Williams, Trever Hines for helpful  
468 instructions on the general Maxwell representations of a Burgers rheology. Comments and suggestions by Liangyu Zhu, Lingyun Ji  
469 and two reviewers helped us improve the manuscript. Special thanks to Yehuda Bock for revising the manuscript. We appreciate  
470 Rongjiang Wang, Fred F. Pollitz for providing useful software tools: SDM, PSGRN/PSCMP, and VISCO2.5D. The figures were  
471 generated using GMT software.

#### 472 **Author details**

473 1. State Key Laboratory of Earthquake Dynamics, Institute of Geology, China Earthquake Administration, Beijing, 100029, China

474 2. Shaanxi Earthquake Agency, Xi'an, 710068, China

475 3. Faculty of Geomatics, Lanzhou Jiaotong University, Lanzhou, 730070, China

476

477 **REFERENCE**

- 478 [1]. Aagaard B T , Knepley M G , Williams C A . A domain decomposition approach to implementing fault slip  
479 in finite-element models of quasi-static and dynamic crustal deformation[J]. *Journal of Geophysical Research:*  
480 *Solid Earth*, 2013, 118(6):3059-3079.
- 481 [2]. Ader T , Avouac J P , Liu-Zeng J , et al. Convergence rate across the Nepal Himalaya and interseismic  
482 coupling on the Main Himalayan Thrust: Implications for seismic hazard[J]. *Journal of Geophysical*  
483 *Research*, 2012, 117(B4):398-399.
- 484 [3]. Altamimi, Z., Rebischung, P., Métivier, L., & Collilieux, X. ITRF2014: A new release of the International  
485 Terrestrial Reference Frame modeling nonlinear station motions. *Journal of Geophysical Research: Solid*  
486 *Earth*, 2016,121(8), 6109-6131. Avouac J P, Meng L, Wei S, et al. Lower edge of locked Main Himalayan  
487 Thrust unzipped by the 2015 Gorkha earthquake[J]. *Nature Geoscience*, 2015, 8(9).
- 488 [4]. Bai, D., Unsworth, M.J., Meju, M.A., Ma, X., Teng, J., Kong, X., Sun, Y., Sun, J., Wang, L., Jiang, C., Zhao,  
489 C., Xiao, P., Liu, M. Crustal deformation of the eastern Tibetan plateau revealed by magnetotelluric imaging.  
490 *Nat. Geosci.* 2010,3, 358–362.
- 491 [5]. Barbot S , Hamiel Y , Fialko Y . Space geodetic investigation of the coseismic and postseismic deformation  
492 due to the 2003 Mw7.2 Altai earthquake: Implications for the local lithospheric rheology[J]. *J. Geophys Res.*,  
493 2008, 113, B03403
- 494 [6]. Barbot, S., Fialko Y. and Bock Y., Postseismic deformation due to the Mw6.0 2004 Parkfield earthquake:  
495 Stress-driven creep on a fault with spatially variable rate-and-state friction parameters, *J. Geophys*  
496 *Res.*,2009,114, B07405, doi:10.1029/2008JB005748
- 497 [7]. Barbot et al., A unified continuum representation of postseismic relaxation mechanisms: Semi-analytic  
498 models of afterslip, poroelastic rebound and viscoelastic flow[J], *Geophys. J. Int.*, 2010,182, 1124-1140.
- 499 [8]. Bettinelli P , Avouac J P , Flouzat M , et al. Plate Motion of India and Interseismic Strain in the Nepal  
500 Himalaya from GPS and DORIS Measurements[J]. *Journal of Geodesy*, 2006, 80(8-11):567-589.
- 501 [9]. Blacker, Teddy D., Owen, Steven J., Staten, Matthew L., Quadros, William Roshan, Hanks, Byron, Clark,  
502 Brett W., Meyers, Ray J., Ernst, Corey, Merkley, Karl, Morris, Randy, McBride, Corey, Stimpson, Clinton,  
503 Plooster, Michael, and Showman, Sam. CUBIT Geometry and Mesh Generation Toolkit 15.2 User  
504 Documentation. United States: N. p., 2016. Web. doi:10.2172/1457612.
- 505 [10]. Blewitt, G., Hammond, W. C., & Kreemer, C. Harnessing the GPS data explosion for interdisciplinary  
506 science. *Eos*, 2018,99, 1-2.
- 507 [11]. Bilham R, Larson K, Freymueller J. GPS measurements of present-day convergence across the Nepal  
508 Himalaya[J]. *Nature*, 1997, 386(6620):61- 64.
- 509 [12]. Bilham R. Earthquakes in India and the Himalaya: tectonics, geodesy and history[J]. *Annals of Geophysics*,

510 2004, 47(2-3):839-858.

511 [13]. Bollinger L , Avouac J P , Cattin R , et al. Stress buildup in the Himalaya[J]. Journal of Geophysical  
512 Research: Solid Earth, 2004, 109(B11),doi:10.1029/2003JB002911.

513 [14]. Cattin R , Avouac J P . Modeling mountain building and the seismic cycle in the Himalaya of Nepal[J].  
514 Journal of Geophysical Research, 2000, 105(B6):13389.

515 [15]. Cattin R , Martelet G , Henry P , et al. Gravity anomalies, crustal structure and thermo-mechanical support of  
516 the Himalaya of Central Nepal[J]. Geophysical Journal of the Royal Astronomical Society, 2001,  
517 147(2):381-392.

518 [16]. Diao F , Xiong X , Wang R , et al. Overlapping post-seismic deformation processes: afterslip and viscoelastic  
519 relaxation following the 2011 Mw 9.0 Tohoku (Japan) earthquake[J]. Geophysical Journal International,  
520 2014, 196(1):218-229.

521 [17]. Elliott, J. R., Jolivet, R., González, P. J., Avouac, J. P., Hollingsworth, J., Searle, M. P., & Stevens, V.  
522 L..Himalayan megathrust geometry and relation to topography revealed by the Gorkha earthquake. Nature  
523 Geoscience, 2016,9(2), 174–180.

524 [18]. Fialko, Y., Evidence of fluid-filled upper crust from observations of post-seismic deformation due to the  
525 1992 Mw7.3 Landers earthquake, J. Geophys. Res., 2004,109, B08401.

526 [19]. Feng, G., Li, Z., Shan, X., Zhang, L., Zhang, G., Zhu, J.. Geodetic model of the 2015 pril 25 Mw7.8 Gorkha  
527 Nepal Earthquake and Mw7.3 aftershock estimated from InSAR and GPS data. Geophys. J. Int. , 2015, 203,  
528 896–900.

529 [20]. Freed A M, Bürgmann R. Evidence of power-law flow in the Mojave desert mantle[J]. Nature, 2004,  
530 430(6999):548-51

531 [21]. Freed A M, Bürgmann R, Herring T. Far-reaching transient motions after Mojave earthquakes require broad  
532 mantle flow beneath a strong crust[J]. Geophysical Research Letters, 2007, 34(19):228-262.

533 [22]. Freed A M, Ali S T, Bürgmann R. Evolution of stress in Southern California for the past 200 years from  
534 coseismic, postseismic and interseismic stress changes[J]. Geophysical Journal of the Royal Astronomical  
535 Society, 2010, 169(3):1164-1179.

536 [23]. Freed A M, Hashima A, Becker T W, et al. Resolving depth-dependent subduction zone viscosity and  
537 afterslip from postseismic displacements following the 2011 Tohoku-oki, Japan earthquake[J]. Earth and  
538 Planetary Science Letters, 2017: 279-290.

539 [24]. Fu Y , Freymueller J T . Seasonal and long-term vertical deformation in the Nepal Himalaya constrained by  
540 GPS and GRACE measurements[J]. Journal of Geophysical Research: Solid Earth, 2012, 117(B3).  
541 <https://doi.org/10.1029/2011JB008925>

542 [25]. Galetzka J, Melgar D, Genrich JF, et al. Slip pulse and resonance of the Kathmandu basin during the 2015  
543 Gorkha earthquake, Nepal.[J]. Science, 2015, 349(6252):1091-1095.

544 [26]. Gonzalez-Ortega A, Fialko Y, Sandwell D, et al. El Mayor-Cucapah (Mw 7.2) earthquake: Early near-field  
545 postseismic deformation from InSAR and GPS observations[J]. Journal of Geophysical Research Solid Earth,

2014, 119(2):1482-1497

[27]. Gualandi, A., Avouac, J.-P., Galetzka, J., Genrich, J. F., Blewitt, G., Adhikari, L. B., Liu-Zeng, J. Pre- and post-seismic deformation related to the 2015, Mw 7.8 Gorkha earthquake, Nepal. *Tectonophysics*, 2016, 714–715, 90–106

[28]. Hetényi, G., Cattin, R., Vergne, J., Nábělek, J.L.. The effective elastic thickness of the India Plate from receiver function imaging, gravity anomalies and thermomechanical modelling. *Geophys. J. Int.* , 2006, 167, 1106–1118.

[29]. Hines, T.T., Hetland, E.A., Rapid and simultaneous estimation of fault slip and heterogeneous lithospheric viscosity from post-seismic deformation. *Geophys. J. Int.* 2016, 204, 569–582.

[30]. Hsu Y J, Simons M, Avouac J P, et al.. Frictional Afterslip Following the 2005 Nias-Simeulue Earthquake, Sumatra[J]. *Science*, 2006, 312(5782):1921

[31]. Hsu Y , Simons M , Williams C , et al. Three-dimensional FEM derived elastic Green's functions for the coseismic deformation of the 2005 Mw8.7 Nias-Simeulue, Sumatra earthquake[J]. *Geochemistry Geophysics Geosystems*, 2013, 12(7)

[32]. Hu Y, Bürgmann, Roland, Freymueller, Jeffrey T, et al. Contributions of poroelastic rebound and a weak volcanic arc to the postseismic deformation of the 2011 Tohoku earthquake[J]. *Earth Planets & Space*, 2014, 66(1):106.

[33]. Hu Y , Bürgmann, Roland, Banerjee P , et al. Asthenosphere rheology inferred from observations of the 2012 Indian Ocean earthquake[J]. *Nature*, 2016. <https://doi.org/10.1038/nature19787>

[34]. Huang, M.-H., Bürgmann, R., Freed, A.M. Probing the lithospheric rheology across the eastern margin of the Tibetan Plateau. *Earth Planet. Sci. Lett.* , 2014, 396, 88 – 96.

[35]. Hughes KLH, Masterlark T, Mooney WD: Poroelastic stress-triggering of the 2005 M8.7 Nias earthquake by the 2004 M9.2 Sumatra - Andaman earthquake. *Earth Planet Science Letter*, 2010, 293(3 - 4):289 - 299. doi: 10.1016/j.epsl.2010.02.043

[36]. Johnston, G., Riddell, A., & Hausler, G. The international GNSS service. 2017, In *Springer handbook of global navigation satellite systems* (pp. 967-982). Springer, Cham.

[37]. Jouanne F , Gajurel A , Mugnier J L , et al. Postseismic deformation following the April 25, 2015 Gorkha earthquake (Nepal): Afterslip versus viscous relaxation[J]. *Journal of Asian earth Sciences*, 2019, 176(JUN.1):105-119.

[38]. Jiang G , Wang Y , Wen Y , et al. Afterslip evolution on the crustal ramp of the Main Himalayan Thrust fault following the 2015 Mw 7.8 Gorkha (Nepal) earthquake[J]. *Tectonophysics*, 2019, 758:29-43.

[39]. Jiang, Z., Yuan, L., Huang, D., Yang, Z., & Hassan, A. Postseismic deformation associated with the 2015 mw 7.8 gorkha earthquake, nepal: investigating ongoing afterslip and constraining crustal rheology. *Journal of Asian Earth Sciences*. 2018, DOI:10.1016/j.jseas.2017.12.039

[40]. Klein E, Fleitout L, Vigny C, et al. Afterslip and viscoelastic relaxation model inferred from the large-scale

581 post-seismic deformation following the 2010 Mw 8.8 Maule earthquake (Chile)[J]. *Geophysical Journal*  
582 *International*, 2016, 205(3): 1455-1472.

583 [41]. Kyriakopoulos, C., T. Masterlark, S. Stramondo, M. Chini, and C. Bignami. Coseismic slip distribution for  
584 the Mw 9 2011 Tohoku-Oki earthquake derived from 3-D FE modeling, *J. Geophys. Res. Solid Earth*,  
585 2013 ,118, 3837 – 3847

586 [42]. Kumar S, Wesnousky SG, Rockwell TK, et al. Earthquake recurrence and rupture dynamics of Himalayan  
587 Frontal Thrust, India.[J]. *Science*, 2001, 294(5550): 2328-2331.

588 [43]. Laske, G., Masters, G., Ma, Z. & Pasyanos, M. E. CRUST1.0: an updated global model of Earth' s crust.  
589 *Geophys. Res. Abstr.* 15, Abstract EGU2013 – 2658 (2013).

590 [44]. Lavé, J., & Avouac, J.-P. Active folding of fluvial terraces across the Siwaliks Hills, Himalayas of Central  
591 Nepal. *Journal of Geophysical Research*, 2000,105(B3), 5735 – 5770. <https://doi.org/10.1029/1999JB900292>

592 [45]. Lindsey, E. O., Natsuaki, R., Xu, X., Shimada, M., Hashimoto, M., Melgar, D., & Sandwell, D. T. Line-of-  
593 sight displacement from ALOS-2 interferometry: Mw 7.8 Gorkha earthquake and Mw 7.3 aftershock.  
594 *Geophysical Research Letters*, 2015,42, 6655–6661. <https://doi.org/10.1002/2015GL065385>

595 [46]. Lienkaemper, J.J., McFarland, F.S., 2017. Long-term afterslip of the 2004 M 6.0 parkfield, California,  
596 earthquake – implications for forecasting amount and duration of afterslip on other major creeping faults.  
597 *Bulletin of the Seismological Society of America.* 107,1082–1093

598 [47]. Liu, C., Zheng, Y., Wang, R., Shan, B., Xie, Z., Xiong, X., Ge, C. Rupture processes of the 2015 Mw 7.9  
599 Gorkha earthquake and its Mw 7.3 aftershock and their implications on the seismic risk. *Tectonophysics*,  
600 2016, 682, 264–277.

601 [48]. Liu J., Ji C., Zhang J., et al. Tectonic setting and general features of coseismic rupture of the 25 April, 2015  
602 Mw 7.8 Gorkha ,Nepal earthquake (in Chinese). *Chin Sci Bull*, 2015, 60:26 40 – 2655,doi:  
603 10.1360/N972015 -00559

604 [49]. Liu J., Zhang Z , Rollins C , et al. Postseismic deformation following the 2015 Mw7.8 Gorkha (Nepal)  
605 earthquake: new GPS data, kinematic and dynamic models, and the roles of afterslip and viscoelastic  
606 relaxation[J]. *Journal of Geophysical Research: Solid Earth*, 2020.

607 [50]. Marone C.J., Scholz C.H., Bilham R. On the mechanics of earthquake afterslip[J]. *J Geophys Res.*, 1991,  
608 96:8441-8452

609 [51]. Masterlark, T., C. DeMets, H. Wang, O. Sanchez, and J. Stock. Homogeneous vs heterogeneous subduction  
610 zone models: Coseismic and postseismic deformation, *Geophys. Res. Lett.*, 2001,28(21), 4047–4050,  
611 doi:10.1029/2001GL013612.

612 [52]. Masterlark, T. Finite element model predictions of static deformation from dislocation sources in a  
613 subduction zone: Sensitivities to homogeneous, isotropic, Poisson-solid, and half-space assumptions, *J.*  
614 *Geophys. Res.*,2003, 108(B11), 2540, doi:10.1029/2002JB002296.

615 [53]. Masterlark, T., K. L. Feigl, M. Haney, J. Stone, C. Thurber, and E. Ronchin. Nonlinear estimation of

616 geometric parameters in FEMs of volcano deformation: Integrating tomography models and geodetic data for  
617 Okmok volcano, Alaska, *J. Geophys. Res.*, 2012, 117, B02407, doi:10.1029/2011JB008811.

618 [54]. Mencin, D., Bendick, R., Upreti, B. N., Adhikari, D. P., Gajurel, A. P., Bhattarai, R. R., Bilham, R.  
619 Himalayan strain reservoir inferred from limited afterslip following the Gorkha earthquake. *Nature*  
620 *Geoscience*, 2016, 9, 533–537. <https://doi.org/10.1038/ngeo27344>

621 [55]. Monsalve, G., Sheehan, A., Schulte-Pelkum, V., Rajaure, S., Pandey, M., & Wu, F. Seismicity and one-  
622 dimensional velocity structure of the Himalayan collision zone: Earthquakes in the crust and upper mantle.  
623 *Journal of Geophysical Research*, 2006, 111, B10301. <https://doi.org/10.1029/2005JB004062>

624 [56]. Nikolaidis R. M. Observation of geodetic and seismic deformation with the global positioning system [D].  
625 Univ. of Calif., San Diego, 2002.

626 [57]. Paul Segall., *Earthquake and volcano deformation* [M]. Princeton University Press, 2010.

627 [58]. Peltzer G, Rosen P, Rogez F, et al. Poroelastic rebound along the Landers 1992 earthquake surface  
628 rupture [J]. *Journal of Geophysical Research Atmospheres*, 1998, 1033(B12):30131-30146

629 [59]. Perfettini H, Avouac J -. Postseismic relaxation driven by brittle creep: A possible mechanism to reconcile  
630 geodetic measurements and the decay rate of aftershocks, application to the Chi-Chi earthquake, Taiwan [J].  
631 *Journal of Geophysical Research Solid Earth*, 2004, 109(B2)

632 [60]. Pollitz F, Vergnolle M, Calais E. Fault Interaction and Stress Triggering of 20th Century Earthquakes in  
633 Mongolia [J]. *Journal of Geophysical Research Solid Earth*, 2003, 108(B10)

634 [61]. Pollitz, F.F., 2014. Post-earthquake relaxation using a spectral element method: 2.5- D case. *Geophys. J. Int.*  
635 198, 308–326

636 [62]. Pratama, C., Ito, T., Sasajima, R., Tabei, T., et al. Transient rheology of the oceanic asthenosphere following  
637 the 2012 Indian Ocean earthquake inferred from geodetic data. *Journal of Asian Earth Sciences*, 2017, 147.

638 [63]. Qiu, Q., Hill, E. M., Barbot, S., Hubbard, J., Feng, W., Lindsey, E. O., Tapponnier, P. The mechanism of  
639 partial rupture of a locked megathrust: The role of fault morphology. *Geology*, 2016, 44(10), 875–878.  
640 <https://doi.org/10.1130/G38178.1>

641 [64]. Reischung, P., Griffiths, J., Ray, J., Schmid, R., Collilieux, X., & Garayt, B. IGS08: the IGS realization of  
642 ITRF2008. *GPS solutions*, 2012, 16(4), 483-494.

643 [65]. Rousset, B., Barbot, S., Avouac, J.-P., & Hsu, Y.-J. Postseismic deformation following the 1999 Chi-Chi  
644 earthquake, Taiwan: Implication for lower-crust rheology. *Journal of Geophysical Research*, 2012, 117,  
645 B12405. <https://doi.org/10.1029/2012JB009571>

646 [66]. Ryder, I., Bürgmann, R., Pollitz, F. Lower crustal relaxation beneath the Tibetan Plateau and Qaidam Basin  
647 following the 2001 Kokoxili earthquake. *Geophys. J. Int.*, 2011, 187, 613–630

648 [67]. Sapkota S N, Bollinger L, Klinger Y, et al. Primary surface ruptures of the great Himalayan earthquakes in  
649 1934 and 1255 [J]. *Nature Geoscience*, 2013, 6(2):152-152.

650 [68]. Savage, J., and J. Svarc. Postseismic relaxation following the 1992 M7.3 Landers and 1999 M7.1 Hector  
651 Mine earthquakes, southern California [J]. *J. Geophys. Res.*, 2009, 114, B01401, doi:10.1029/2008JB005938

- 652 [69]. Schulte-Pelkum, V., Monsalve, G., Sheehan, A., Pandey, M. R., Sapkota, S., Bilham, R., & Wu, F. Imaging  
653 the Indian subcontinent beneath the Himalaya. *Nature*, 2005,435(7046), 1222–1225.  
654 <https://doi.org/10.1038/nature03678>
- 655 [70]. Shen, Z., Jackson, D. D., Feng, Y., Cline, M. W., Kim, M., Fang, P., & Bock, Y. Postseismic Deformation  
656 Following the Landers Earthquake, California, 28 June 1992. *Bulletin of the Seismological Society of*  
657 *America: Special Issue on the Landers Earthquake Sequence*, 1994,84(3), 780-791
- 658 [71]. Sreejith, K., Sunil, P., Agrawal, R., Saji, A. P., Ramesh, D., & Rajawat, A. Coseismic and early postseismic  
659 deformation due to the 25 April 2015, Mw7.8 Gorkha, Nepal, earthquake from InSAR and GPS  
660 measurements. *Geophysical Research Letters*, 2016,43(7), 3160–3168
- 661 [72]. Stevens, V. L., & Avouac, J.-P. Interseismic coupling on the Main Himalayan thrust. *Geophysical Research*  
662 *Letters*, 2015, 42, 5828–5837. <https://doi.org/10.1002/2015GL064845>
- 663 [73]. Su, X.; Yao, L.; Wu, W.; Meng, G.; Su, L.; Xiong, R.; Hong, S. Crustal Deformation on the Northeastern  
664 Margin of the Tibetan Plateau from Continuous GPS Observations. *Remote Sens.* 2019, 11, 34.
- 665 [74]. Suito H. Importance of rheological heterogeneity for interpreting viscoelastic relaxation caused by the 2011  
666 Tohoku-Oki earthquake[J]. *Earth, Planets and Space*, 2017, 69(1).
- 667 [75]. Sun Y , Dong S , Zhang H , et al. 3D thermal structure of the continental lithosphere beneath China and  
668 adjacent regions[J]. *Journal of Asian Earth Sciences*, 2013, 62:697-704.
- 669 [76]. Tung, S., and T. Masterlark. Coseismic slip distribution of the 2015 Mw7.8 Gorkha, Nepal, earthquake from  
670 joint inversion of GPS and InSAR data for slip within a 3-D heterogeneous Domain, *J. Geophys. Res. Solid*  
671 *Earth*, 2016, 121, 3479–3503, doi:10.1002/2015JB012497.
- 672 [77]. U.S. Geological Survey (USGS) (2015), USGS National Earthquake Information Center
- 673 [78]. Wang, K., Fialko, Y.. Space geodetic observations and models of postseismic deformation due to the 2005  
674 M7. 6 Kashmir (Pakistan) earthquake. *J. Geophys. Res. Solid Earth*, 2014, 119, 7306–7318
- 675 [79]. Wang, K., Fialko, Y.. Slip model of the 2015 Mw7.8 Gorkha (Nepal) earthquake from inversions of ALOS-2  
676 and GPS data. *Geophys. Res. Lett.* , 2015, 42, 7452–7458.
- 677 [80]. Wang, K., & Fialko, Y. Observations and modeling of coseismic and postseismic deformation due to the  
678 2015 Mw 7.8 Gorkha (Nepal) earthquake. *Journal of Geophysical Research: Solid Earth*,  
679 2018.123. <https://doi.org/10.1002/2017JB014620>
- 680 [81]. Wang R. SDM - A geodetic inversion code incorporating with layered crust structure and curved fault  
681 geometry[C]// Egu General Assembly Conference. 2013.
- 682 [82]. Wang, R., & Kümpel, H.-J. Poroelasticity: Efficient modeling of strongly coupled, slow deformation  
683 processes in a multilayered half-space. *Geophysics*, 2003,68(2), 705–717.
- 684 [83]. Wang, R., Lorenzo-Martín, F., & Roth, F. PSGRN/PSCMP—A new code for calculating co- and post-  
685 seismic deformation, geoid and gravity changes based on the viscoelastic-gravitational dislocation theory.  
686 *Computers & Geosciences*, 2006, 32(4), 527–541. <https://doi.org/10.1016/j.cageo.2005.08.006>
- 687 [84]. Wen, Y., Li, Z., Xu, C., Ryder, I., Bürgmann, R.. Postseismic motion after the 2001 Mw 7.8 Kokoxili

688 earthquake in Tibet observed by InSAR time series. *J. Geophys. Res. Solid Earth* , 2012,117  
689 [85]. Wiseman K, Burgmann R, Freed A M, et al. Viscoelastic relaxation in a heterogeneous Earth following the  
690 2004 Sumatra-Andaman earthquake[J]. *Earth and Planetary Science Letters*, 2015: 308-317.  
691 [86]. Wessel, P., Luis, J. F., Uieda, L., Scharroo, R., Wobbe, F., Smith, W. H. F., & Tian, D. The Generic  
692 Mapping Tools version 6. *Geochemistry, Geophysics, Geosystems*, 2019,20, 5556–5564.  
693 [87]. Zhao, B., Bürgmann, R., Wang, D., Tan, K., Du, R., & Zhang, R. Dominant controls of downdip afterslip  
694 and viscous relaxation on the postseismic displacements following the Mw7.9 Gorkha, Nepal, earthquake,  
695 2017,122, 8376–8401. doi.org/10.1002/2017JB014366  
696 [88]. Zhang G., Hetland E, Shan X., Slip in the 2015 Mw 7.9 Gorkha and Mw 7.3 Kodari, Nepal, Earthquakes  
697 Revealed by Seismic and Geodetic Data: Delayed Slip in the Gorkha and Slip Deficit between the Two  
698 Earthquakes. *Seismological Research Letters*, 2015, 86 (6): 1578-1586. <https://doi.org/10.1785/0220150139>  
699

# Figures

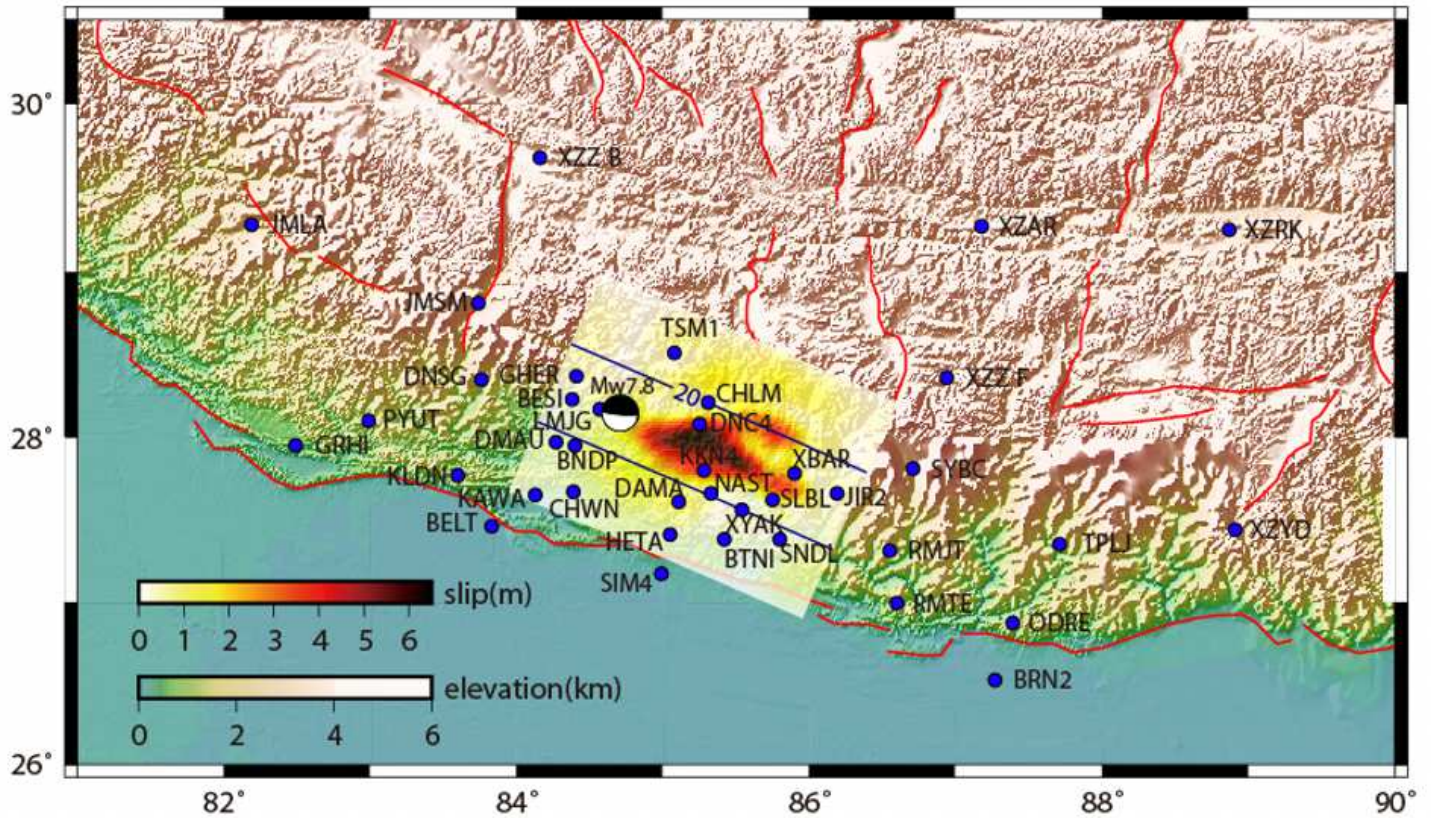


Figure 1

Tectonic setting. The black beach ball shows the mainshock focal mechanism from U.S. Geological Survey. The blue circles are continuous GPS sites used in this study. The color represents the topographical relief, and the color of overlapped fault plane represents the coseismic slip distribution from Tung et al. (2016). The black lines mark the depth of faulting. The red lines represent active faults from Taylor and Yin (2009).

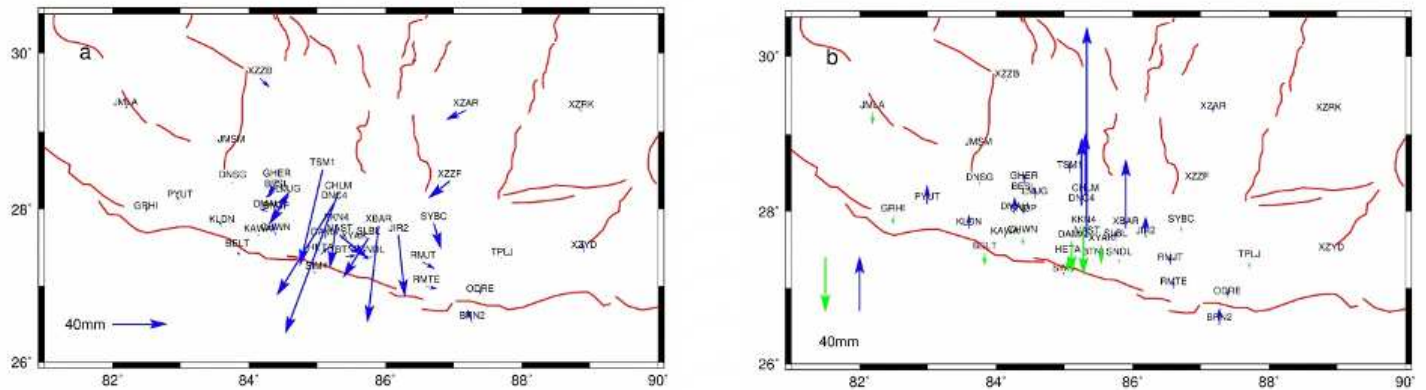
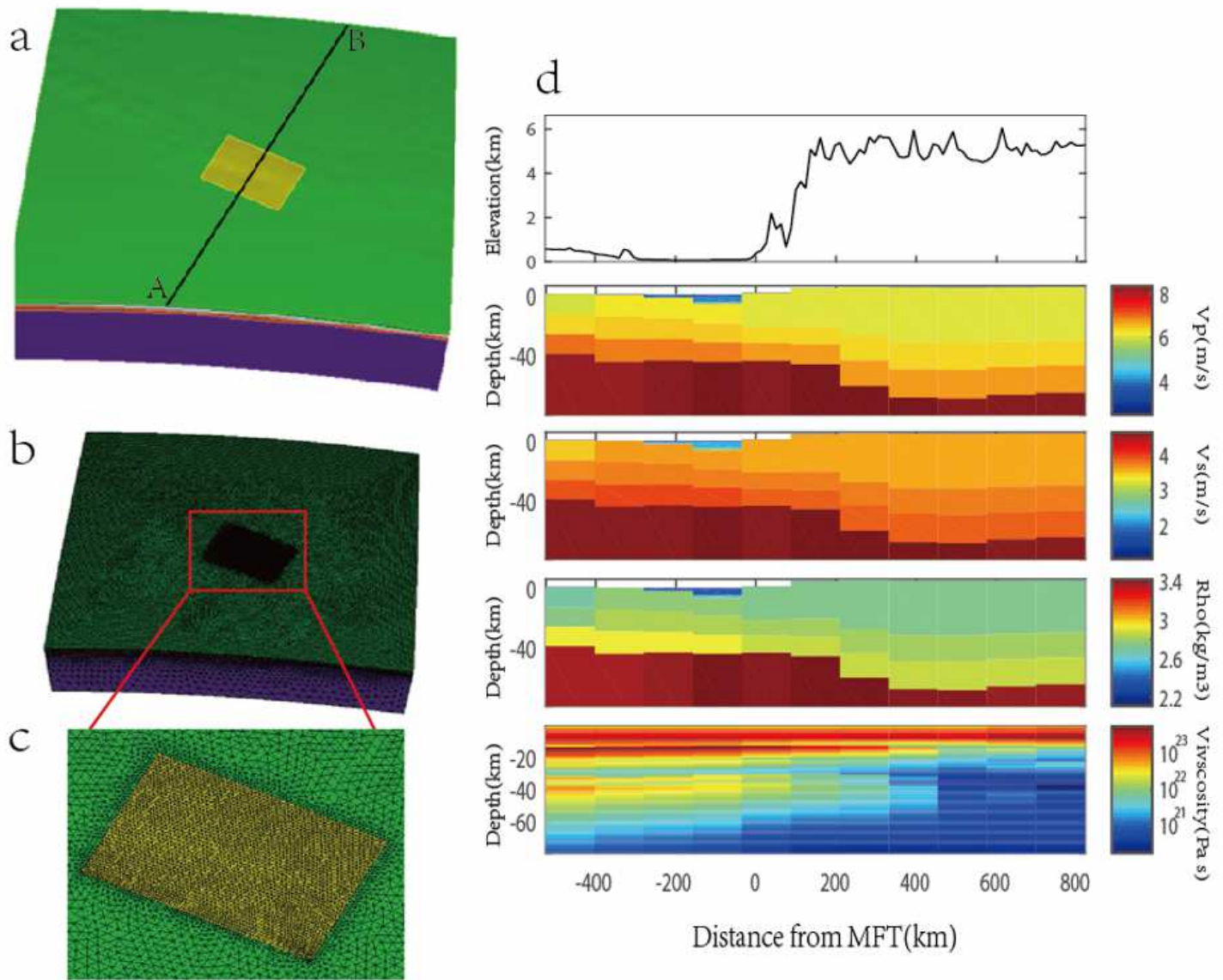


Figure 2

The cumulative horizontal (a) and vertical (b) postseismic displacements exacted from GPS displacement time series. The red lines represent active faults.



**Figure 3**

FEM structure used in the numerical simulation. (a) The yellow rectangle denotes fault rupture. The top surface exhibits topographical relief. The color blocks denote the upper, middle and lower crust and the mantle, respectively. The profile AB is normal to the MFT. (b) Map view of the FEM mesh. (c) The larger view of the FEM mesh in the near-field area of the Gorkha earthquake. (d) The elevation,  $V_p$ ,  $V_s$ , density and viscosity variations along the profile AB. The black line is the source rupture plane.

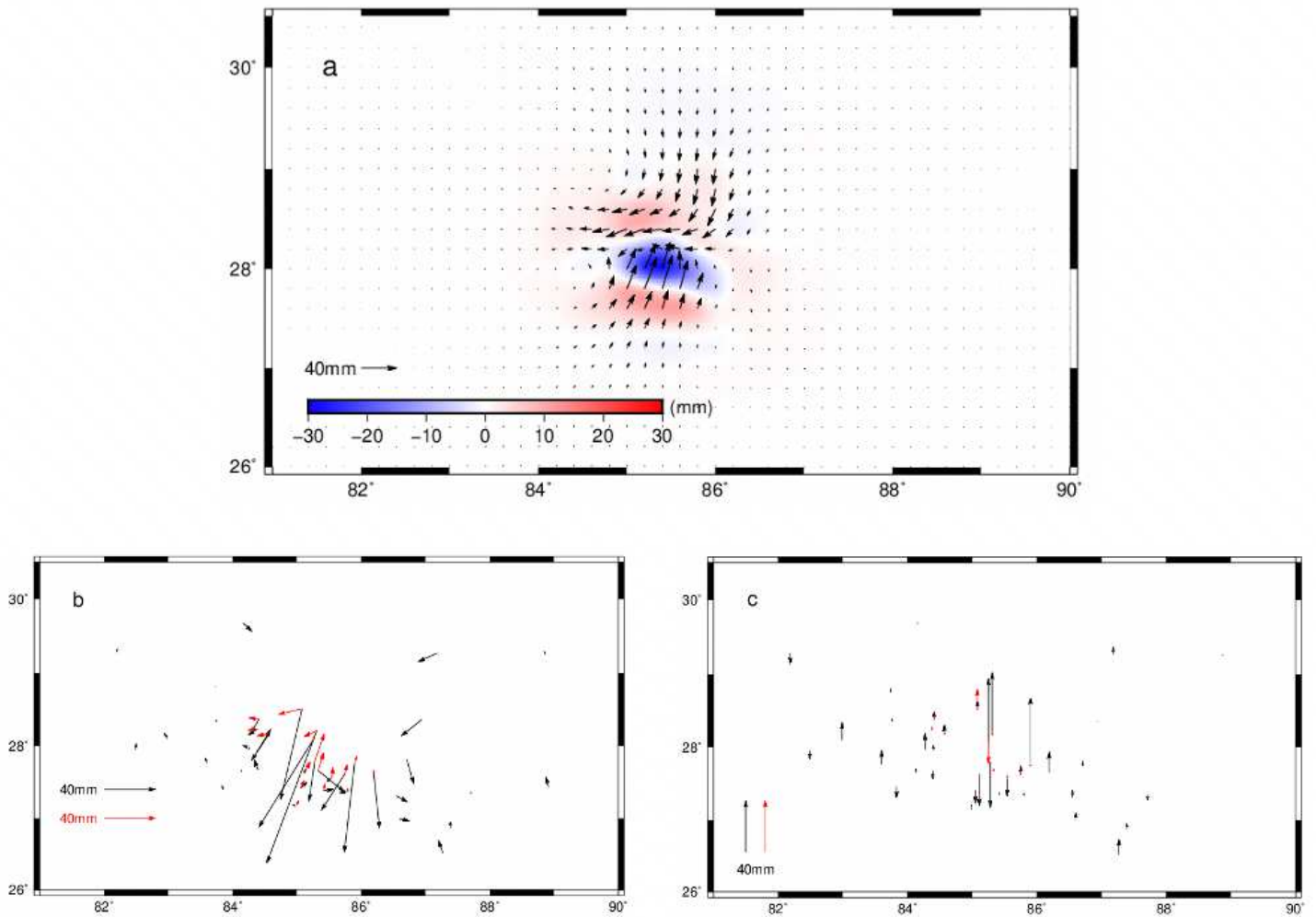


**Figure 4**

The predicted postseismic displacements due to a bi-viscoelastic Burgers model. (a) The color scale represents the vertical component, and the black arrows represent the horizontal component. (b) The comparison between the predicted viscoelastic relaxation (red arrows) and observations (blue arrows) in the horizontal component and (c) the vertical component. The dark blue contours denote the coseismic slip distribution on the fault.

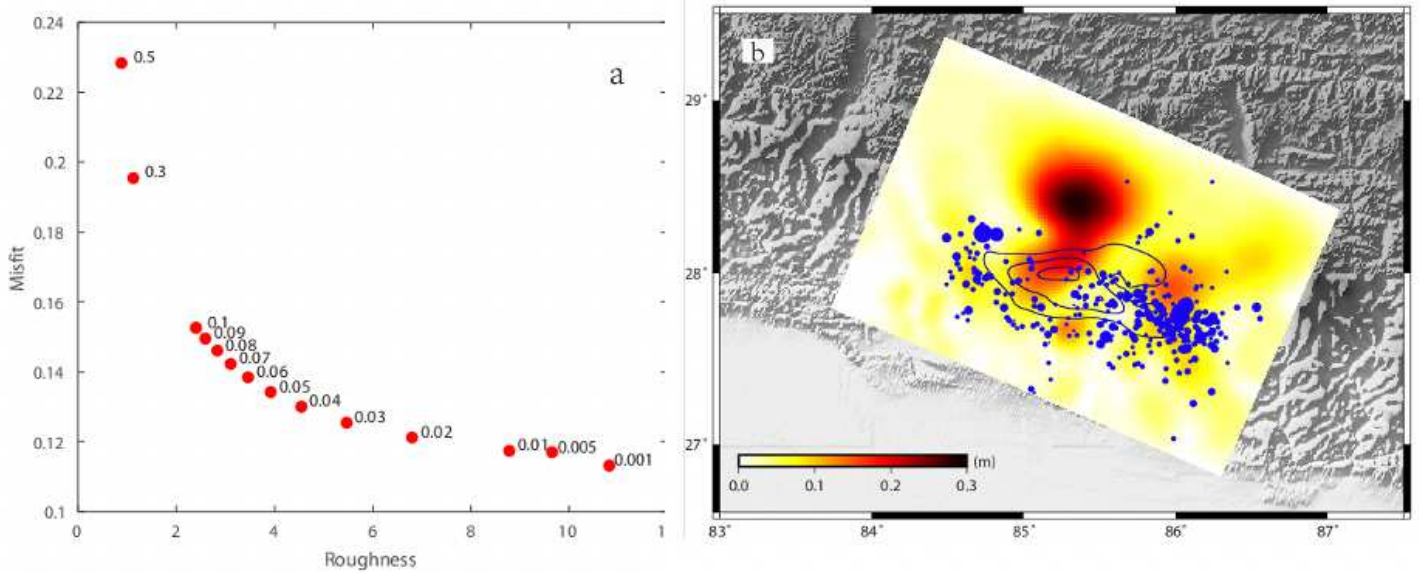


**Figure 5**

(a) Trade-off curve between model roughness and misfit. Numbers indicate the smoothing factor  $\beta$ . (b) The inverted afterslip distribution. The color scale denotes the inverted afterslip distribution. The black contours denote the coseismic slip distribution on the fault. The blue circles denote the aftershocks after the Gorkha earthquake, and the size indicates the magnitude.

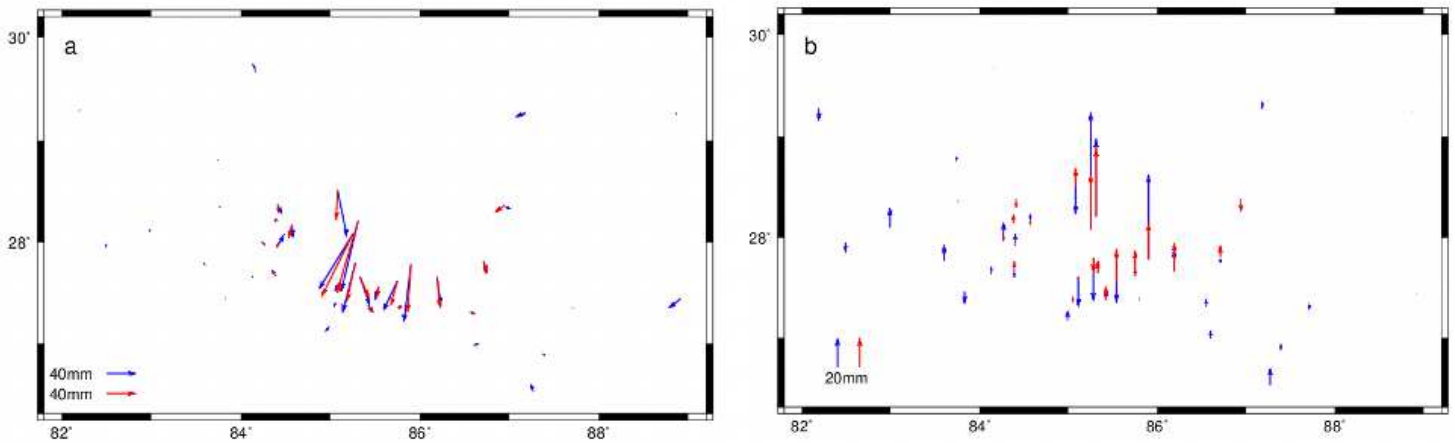


**Figure 6**

The observed postseismic displacement (blue arrows) and predicted postseismic displacement (red arrows) due to afterslip. The dark blue and dark red contours denote the coseismic slip and afterslip distribution on the fault.

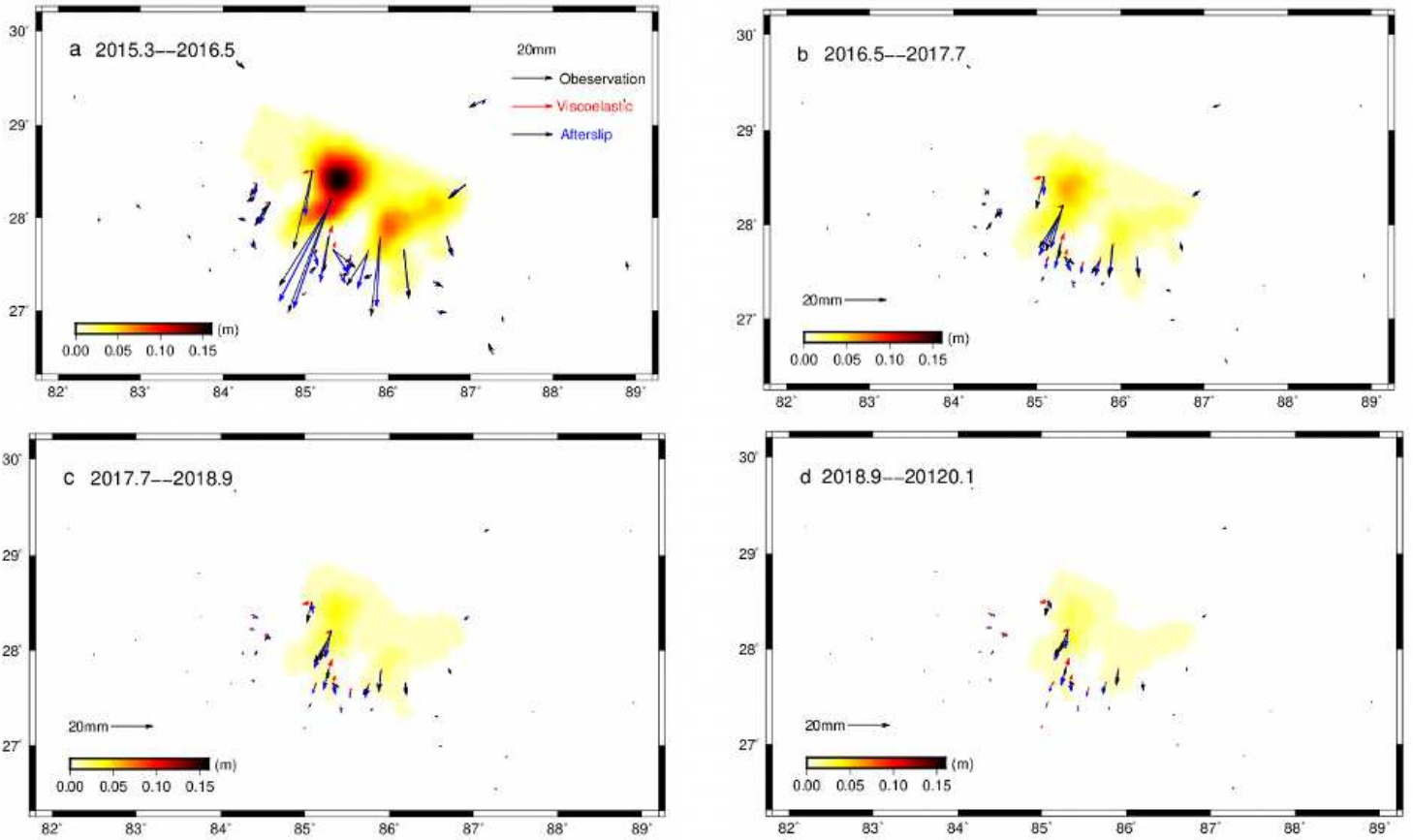


**Figure 7**

Comparisons of observed and calculated displacements, including contributions from viscoelastic relaxation and afterslip during the different periods. Horizontal displacements are presented by arrows. The color Inset in each panel shows horizontal residuals. The dark blue contours denote the coseismic slip distribution on the fault.

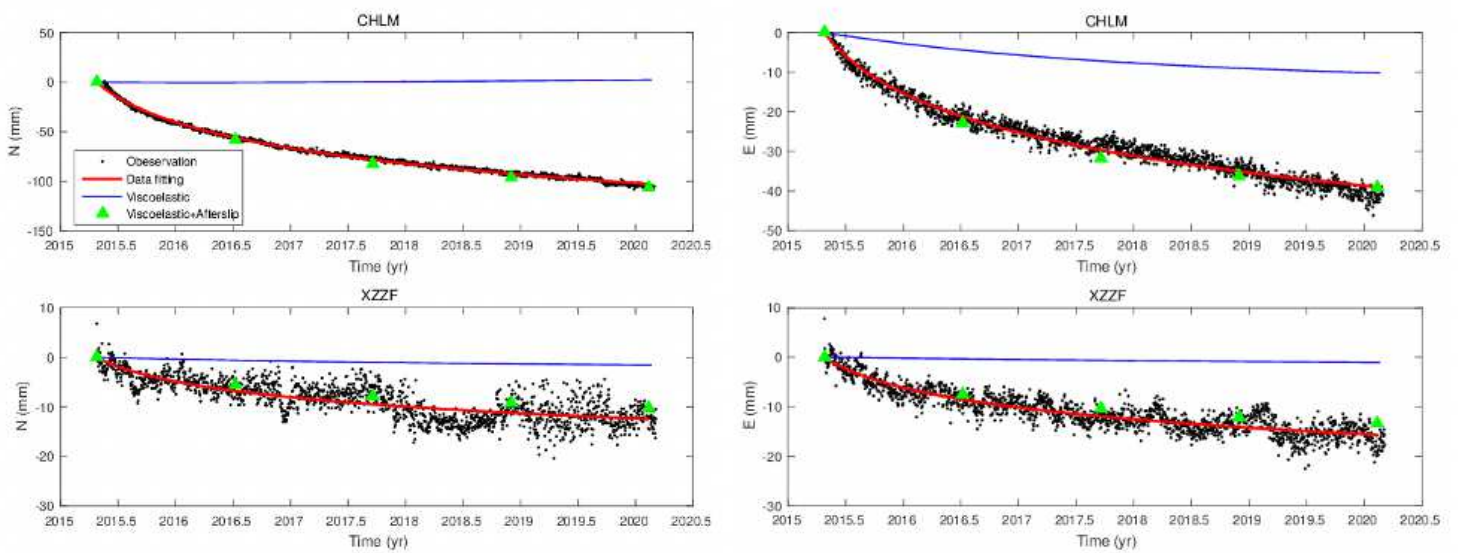


**Figure 8**

The postseismic deformation daily displacement time series of the north and east components at GPS sites CHLM and XZZF. Black dots indicate the observed displacements. The red line indicates the data fitting of the postseismic deformation (Equation 1). The blue line indicates the predicted viscoelastic relaxation. The green triangles indicate the sum of predicted viscoelastic relaxation and the postseismic deformation due to afterslip.

## Supplementary Files

This is a list of supplementary files associated with this preprint. Click to download.

- [SUPPORTINGINFORMATIONclean.docx](#)
- [GraphicalAbstract.docx](#)